Master's thesis

Towards fluorescence upconversion spectroscopy of WS_2 monolayers

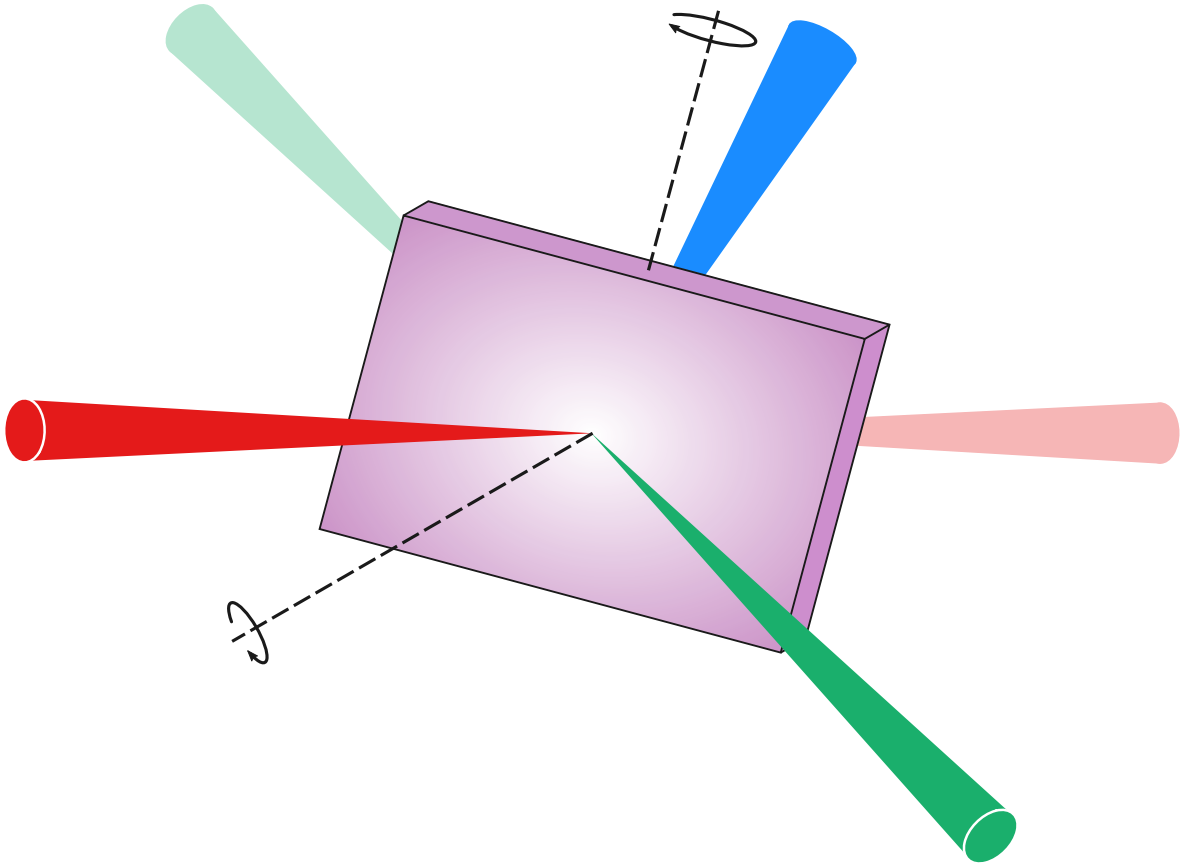

submitted by
Marco Kapitzke

Prof. Julia Stähler
Humboldt-Universität zu Berlin
Prof. Beate Paulus
Freie Universität Berlin

Towards fluorescence upconversion spectroscopy of WS_2 monolayers

by

Marco Kapitzke

Freie Universität Berlin, 2022

A master's thesis submitted in partial fulfillment of
the requirements for the degree of

Master of Science

This thesis was developed in the electron dynamiX group
under the the supervison of Prof. Julia Stähler
at the Department of Chemistry of Humboldt-Universität zu Berlin.

Examining board:

Prof. Julia Stähler
Humboldt-Universität zu Berlin, Department of Chemistry

Prof. Beate Paulus
Freie Universität Berlin, Department of Biology, Chemistry, Pharmacy

Contents

List of Figures

1 CHAPTER

Introduction

SINCE the synthesis of graphene in 2004 [1], there has been a drastic increase in interest in atomically thin materials. Inspired by the impressive progress in this area, alternative monolayer (ML) materials were sought that could serve the study of new physicochemical phenomena. In a short time, the field of 2D materials continued to expand rapidly with pioneering studies on ultrathin transition metal dichalcogenides (TMDCs), hexagonal boron nitride, and other graphene analogs. [2] In particular, TMDCs have attracted considerable attention from the scientific community because their properties are complementary to those of graphene. [3] A variety of applications with different functionality have already been demonstrated for these promising materials, for example, in field-effect transistors [4, 5], ultrasensitive photodetectors [3, 6], chemical sensors [7], and in green thin-film solar cells. [8] The outstanding properties of 2D TMDCs and the potential to control these properties through the chemical environment provide a rich platform to investigate a variety of research questions. [9] Therefore, they are widely considered prime candidates for next-generation nano- and optoelectronics applications.

To capitalize on the excellent properties of TMDCs in future applications, a deep understanding of the underlying electronic structure is of utmost importance, which can be probed by optical spectroscopy. For instance, the complete non-equilibrium carrier dynamics of TDMCs have been scrutinized by ultrafast pump-probe absorption and reflectivity experiments. [10, 11, 12] Due to the splendid time resolution of these techniques, complicated many-body femtosecond dynamics have been observed. However, abundant phenomena are probed simultaneously, often displaying overlapping contributions with miscellaneous dynamics, which can usually not be identified from the transient spectra.

In contrast, time-resolved photoluminescence (PL) spectroscopy can selectively monitor emissive states and therefore serves as an ideal complement to conventional pump-probe spectroscopy. Transient emission spectra could be used to separate radiative from non-radiative relaxation channels and help to analyze the pump-probe spectra. However, the temporal resolution of PL spectroscopy is typically limited to a few picoseconds, preventing the investigation of key features immediately after excitation. In fact, ultrafast decay has been reported and attributed to radiative recombination [13, 14], but direct emission measurements of TMDCs on the femtosecond time scale are lacking to this date.

As mentioned above, conventional techniques for the time resolution of PL fail in the sub-picosecond resolution range. Yet, nonlinear laser techniques allow to achieve a time resolution comparable to the pulse duration of the excitation laser. Therefore, the development of advanced and stable lasers with small pulse widths provides access to subpicosecond dynamics.

The most widely used subpicosecond technique is called optical Kerr gating and utilizes the Kerr effect to generate an "ultrafast shutter". Another nonlinear method is based on the phenomenon of sum-frequency generation (SFG) of light and is called fluorescence upconversion spectroscopy (FLUPS). It is less common due to the high experimental requirements, but the superior method because of better time resolution [15], as well as in terms of measurement sensitivity and accuracy. [16] Although used primarily in the context of solute molecules, recent studies also address crystal spectroscopy [17], quantum dots [18], and nanoplatelets. [19]

Objective and outline

Taken together, the literature suggests that FLUPS is the ideal spectroscopic tool for examining the short-lived emission in TMDCs. Therefore, the ultimate aim of this research is to investigate the radiative ("bright") carrier relaxation in TMDC MLs. This objective is approached using FLUPS, as it provides femtosecond time resolution and all findings in the literature indicate that the upconversion of TMDC emission is feasible. The transient emission spectra will identify the currently inaccessible radiative relaxation dynamics, contributing to a comprehensive understanding of the many-body processes in this class of materials. For this purpose, a FLUPS experiment following N. P. Ernsting's design was set up. However, FLUPS is a highly sensitive experiment with various sources of error, therefore its functionality must first be proven before unknown systems can be studied.

Motivated by the extensive literature on the spectral attributes of coumarins, they were chosen as a test subject for verifying the reliability of the commissioned setup.

In a nutshell, this work has two main objectives:

(i) First, to characterize the FLUPS setup and its measurement modes by determining the time-resolved emission of a well-studied laser dye. Congruence of the transient spectra with the literature can be used to prove its operability.

(ii) Second, applying FLUPS to upconvert the PL of a TMDC ML for the first time.

The thesis is divided into four parts and eleven chapters. After this introduction, the second part outlines the theoretical background concerning the processes and analyzed systems of this work, as well as the basics of nonlinear spectroscopy. The third part focuses on experimental details of broadband FLUPS. This includes the FLUPS operating principle, the measurement setup, various specifics regarding broadband SFG, and data analysis. In the results part, a proper performance of the FLUPS is validated by time-resolved measurements of the peak position, bandwidth, and asymmetry of a coumarin dye. Subsequently, an alternative data analysis method is presented that is not reported in the literature. Finally, strong evidence for the upconversion of TMDC PL was found from depletion spectroscopy. Concrete suggestions are established for signal strength optimization to obtain transient spectra.

In conclusion, this thesis provides the first step towards exploring the femtosecond PL response of a TMDC ML. The finding is very encouraging and suggests that by medium-sized setup adjustments, FLUPS of TMDCs is feasible within the near future.

Background

2 CHAPTER

Fluorescence of organic dyes

This chapter presents important concepts in the emission of fluorescence. The first section introduces the fundamentals of PL by introducing the Jablonski diagram and quantifying the relaxation from the excited state to the ground state. In the second section, the solvation dynamics of fluorophores are discussed. Here, the time-dependent Stokes shift is addressed, which is an important observable in ultrafast fluorescence spectroscopy. Finally, the laser dye coumarin 153 that was experimentally investigated is briefly considered.

2.1 Fundamental concepts

LUMINESCENCE is the spontaneous emission of light from any substance and eventuates from electronically excited states. Excitation is often realized by exposure to light with suitable energy, such that the ground state electrons absorb the photons and are promoted to higher electronic levels. Then, luminescence is referred to as PL. A series of different processes can occur between the absorption and emission of light that are best illustrated in a Jablonski diagram.

Jablonski diagramms [20]

According to A. Jablonski, the electronic transitions in numerous organic molecules can generally be described within the framework of a simplified energy-level scheme. It neglects several interactions, such as energy transfer or interactions of the molecule with the solvent.

A typical Jablonski diagram is shown in figure 2.1, depicting the electronic ground state S_0 and the first and second excited singlet states S_1 and S_2. In each of these electronic states, the fluorophores can exist at several vibrational energy levels $v = 0, 1, 2$, etc. The vibronic transitions between electronic states are shown as vertical lines to illustrate the immediacy of light absorption and emission. This is the so-called Frank-Condon [21, 22], which considers the Born-Oppenheimer approximation: [23] Because the nuclei are much heavier than the electrons, a vibronic transition is completed before the nuclei can react and consequently, their distance remains constant.

At room temperature, the thermal energy is insufficient to significantly populate higher-lying vibrational states. Therefore, absorption primarily occurs from the lowest vibrational level $v = 0$. After absorption, an electron is typically excited to a higher vibrational level of S_1. Molecules in the condensed phase rapidly release their vibrational energy to relax to the vibrational ground state. In the case of excitation to S_2, there is commonly an isoenergetic transition from the vibrational ground state to a highly excited vibrational state of S_1. This process is termed internal conversion (IC) and generally happens in 10^{-12} s or less. Radiative depopulation of S_1 to higher excited vibrational levels of S_0 might occur by spontaneous emission of fluorescence photons, which is followed by vibrational relaxation until the thermal equilibrium is reached. Because the fluorescence lifetime is generally on the order of ~10 ns, fluorescence emission ordinarily proceeds from the lowest energy vibrational state of S_1. Therefore, the identical emission spectrum is collected, regardless of the excitation wavelength. This finding is also known as *Kasha's rule*. Because the geometry of the molecule hardly changes throughout electronic transitions, the emission spectrum is frequently a mirror image of the absorption spectrum.

Molecules in the S_1 state may also undergo intersystem crossing (ISC) to their first triplet state T_1. This conversion is spin-forbidden, but molecules containing heavy atoms can relax this prohibition by strong spin-orbit coupling. Emission from T_1 is called phosphorescence and is shifted to longer wavelengths compared to fluorescence.

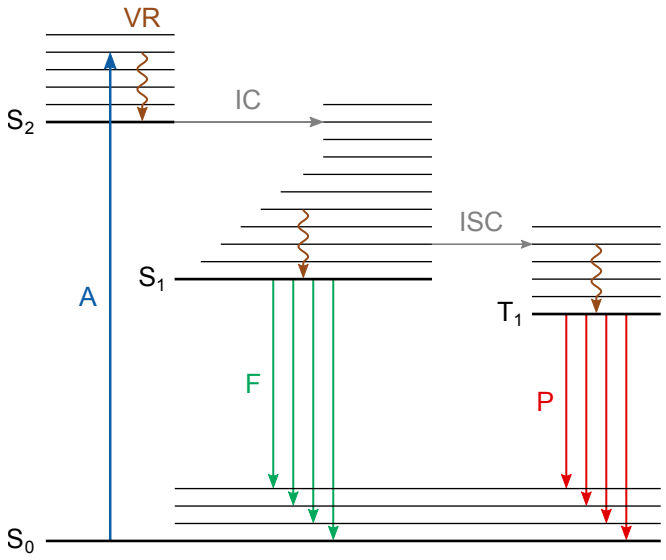

Figure 2.1: Jablonski diagram. The energy-level scheme qualitatively describes possible transitions between different singlet and triplet states of common organic molecules. Abbreviations: A – absorption; VR – vibrational relaxation; F – fluorescence; P – phosphorescence.

Note that the intensity of fluorescence can be decreased by a variety of processes. These are referred to as quenching and are not depicted in the Jablonski diagram (figure 2.1). Quenching can progress through different mechanisms, including collisions, the formation of non-fluorescent complexes, or the inner filter effect. The latter is due to light attenuation by the fluorophore itself and can be reduced by decreasing the sample concentration. [24]

Fluorescence lifetime and quantum yield

Routinely, the fluorescence lifetime $\mathcal{T}$ and quantum yield Q are used as important characteristics of a fluorophore. The meaning of these concepts is best captured by a two-level system that describes the behavior of many fluorophores in good approximation, cf. figure 2.2. The schematic illustrates the relaxation from the excited state S_1 into the ground state S_0. The fluorescence quantum yield is the ratio of emitted to absorbed photons. It is determined by the rate of radiative decay Γ_r and the rate of non-radiative decay Γ_{nr} to the ground state. Mathematically, the quantum yield is accessible via

$$Q = \frac{\Gamma_r}{\Gamma_r + \Gamma_{nr}}. \tag{2.1}$$

Generally, the quantum yield is independent of the excitation wavelength, an observation that is known as *Vavilov's rule*. It is a direct consequence of Kasha's rule.

In the absence of non-radiative relaxation processes, the intrinsic or natural radiative lifetime $\mathcal{T}_\mathrm{r}$ is received:

$$\mathcal{T}_\mathrm{r} = \frac{1}{\Gamma_\mathrm{r}}. \tag{2.2}$$

However, the observed lifetime of an electronic state may be shorter than the radiative lifetime if non-radiative relaxation processes also contribute to depopulating the excited state. In this instance, the quantum yield of the transition $S_1 \rightarrow S_0$ is less than unity. Summing the rates Γ_r and Γ_nr yields the total transition rate whose reciprocal corresponds to the observed lifetime $\mathcal{T}_\mathrm{f}$, which is given by

$$\mathcal{T}_\mathrm{f} = \frac{1}{\Gamma_\mathrm{r} + \Gamma_\mathrm{nr}}. \tag{2.3}$$

For excitation by ultrafast laser pulses, $\mathcal{T}_\mathrm{f}$ can be described by the decrease in the number of excited fluorophores $[F^*(t)]$ as a function of time following optical excitation: [25]

$$\frac{\mathrm{d}[F^*(t)]}{\mathrm{d}t} = -(\Gamma_\mathrm{r} + \Gamma_\mathrm{nr})\left[F^*(t)\right]. \tag{2.4}$$

Because $[F^*(t)]$ is proportional to the emission intensity $I(t)$, integration between $t = 0$ and t shows that the fluorescence decay can be expressed using a single exponential function

$$I(t) = I(t=0)\exp\left(-\frac{t}{\mathcal{T}_\mathrm{f}}\right). \tag{2.5}$$

In this common mono-exponential decay scenario, $\exp(-1) \approx 37\,\%$ of the excitons are still excited at $t = \mathcal{T}_\mathrm{f}$.

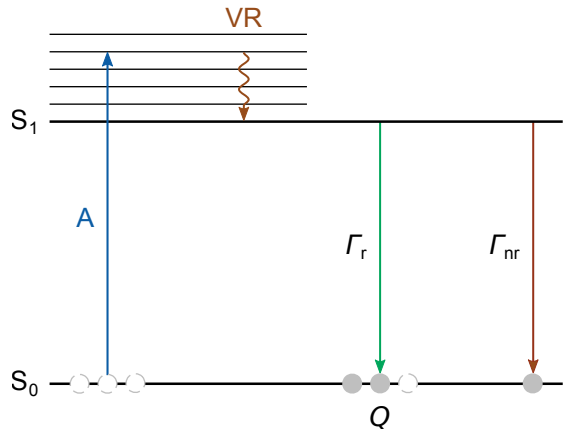

Figure 2.2: Two-level system. In the most elemental consideration, the excited system can return to equilibrium through radiative and non-radiative transitions.

2.2 Solvation dynamics

WHEN a fluorescent molecule is excited from its ground state S_0 to an excited state S_1, the electrons are instantaneously redistributed according to Frank-Condon's principle. The phenomenon of *solvation dynamics* refers to the response of a polar solvent to such a perturbation in charge distribution. The dynamics are illustrated in Figure 2.3.

To begin with, the fluorophore is promoted to its excited state S_1 by the absorption of light (situation 1). Furthermore, consider that the fluorophore undergoes a large change in the dipole moment upon optical excitation. However, the orientation of the solvent is modified with a time delay. Therefore, just after excitation, the solvent molecules are in the perpetual non-equilibrium orientation as before excitation (situation 2). To stabilize the excited state charge distribution in the fluorophore, a polar solvent will relax to its equilibrium configuration on the time scale of picoseconds to femtoseconds. During this process, the energy of the excited state S_1 decreases until a quasi-stationary state is reached. At the same time, the energy of S_0 increases because the solvation shell is optimized for the state S_1 (not shown), i.e. the ground and excited state converge (situation 3). The time-dependence of solvent reorientation can be followed by monitoring the continuous redshift of the fluorescence spectrum that is called time-dependent Stokes shift (TDSS). This shift is a fundamental characteristic of the fluorophore as well as the polar solvent.

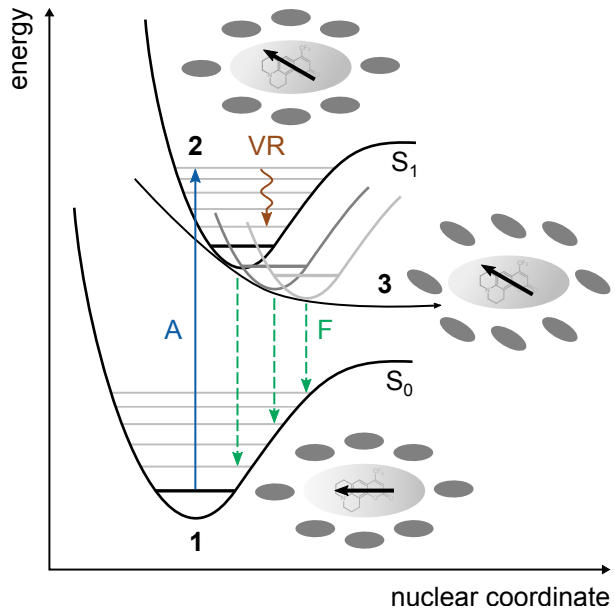

Figure 2.3: Solvation dynamics. Schematic of the processes involved in solvation dynamics: (1) The fluorophore is in its ground state S_0; (2) After excitation, the solvation is still in the Franck-Condon state; (3) Dielectric relaxation brings the system to equilibrium, its evolution is reflected by the TDSS. The figure is adopted from reference [26].

Solvation dynamics of coumarin 153

Due to the delicate assembly of the FLUPS setup, its functionality should be verified before examining novel systems. Motivated by the extensive literature on the solvation dynamics of coumarins, they were chosen as a test subject for the first experiments.

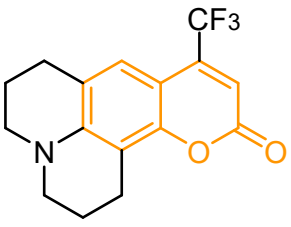

Figure 2.4

Coumarins are conjugated systems that are structurally composed of a benzene ring fused to an α-pyrone ring. The carbonyl group of the pyrone occupies position two. [27] The coumarin parent molecule is highlighted in figure 2.4. Those molecules exhibit interesting fluorescence properties, including high sensitivity to their local environment, especially local polarity. Therefore, the significant solvatochromism of coumarin fluorophores has attracted a lot of attention. [28] In particular, the TDSS of coumarin 153 (C153, see figure 2.4) has been studied extensively, including FLUPS. [29, 30, 31, 32, 33, 34] As a result, C153 has become a benchmark dye in its field.

3 CHAPTER

Transition metal dichalcogenides

This chapter outlines the theoretical background concerning the experimentally investigated TMDC. It opens with a summary of the structural, electronic, and optical properties of its MLs. In the second section, the excitonic properties of the material class are covered in further depth. In particular, the properties that suggest ultrafast radiative relaxation are highlighted.

3.1 Atomically thin TMDCs

CHEMICALLY, each layer of a TMDC MX_2 consists of transition metal atoms M that are sandwiched between two layers of chalcogen atoms X. Especially group VI semiconducting TMDCs with M = Mo, W, and X = S, Se, Te have attracted a lot of attention and only these will be reviewed in the following. Their bulk consists of layered sheets that are held together by interlayer Van-der-Waals forces. TMDCs mainly contain three different allotropes, which lead to different electronic phases: In the thermodynamically stable 2H phase, the metal atom is coordinated trigonally prismatically, whereas the coordination of the metal is octahedral in the 1T phase. Figure 3.1a highlights the unit cell of the 2H phase that belongs to the point group $P\bar{6}m2$. [35]

In such Van-der-Waals systems, the layers can be separated by mechanical exfoliation [36, 4] or liquid exfoliation [37] to isolate single-layer flakes. Alternatively, samples can be prepared using chemical vapor deposition (CVD), where a chemical reaction at the heated substrate surface causes the gaseous sample to be separated as a solid layer. [38]

In 2010, the group of T. F. Heinz demonstrated in a groundbreaking paper that when reduced to a ML, MoS_2 becomes a direct bandgap material [39]. This behavior holds for other TMDCs as well. A direct bandgap enables efficient optoelectronic applications that remain closed to indirect bandgap materials. Hence, a variety of promising applications of TMDCs have already been confirmed, refer to chapter 1 for examples. Figure 3.1b compares the band structure of a bulk (orange) and a 2D TMDC (blue) at the symmetry points K, Γ, and T, respectively.

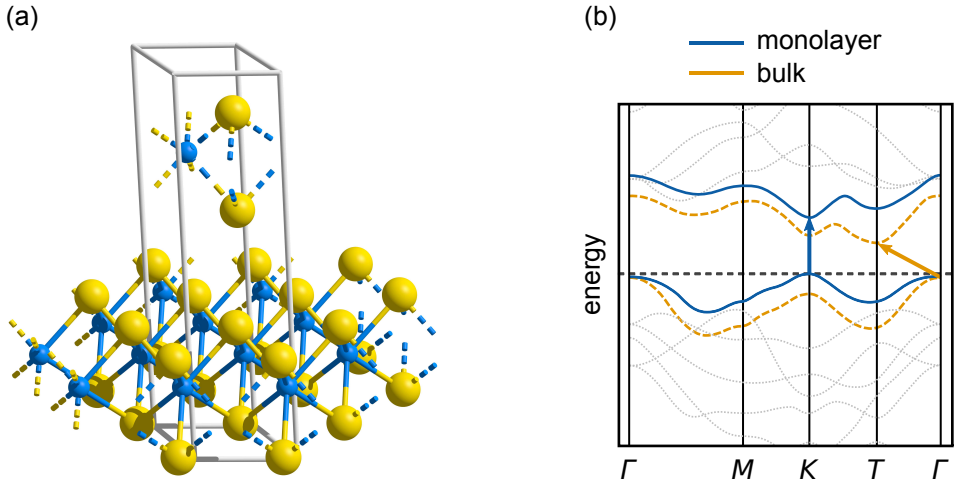

Figure 3.1: Geometric and electronic structure of TMDCs. (a) Structure and unit cell of 2D TMDCs; (b) Schematic of the electronic band structure of a bulk and a 2D TMDC. The figure is adopted from reference [40].

The orbital characteristics of the conduction band (CB) and valence band (VB) are predominantly determined by the d-orbitals of the metal atom: d_{z^2} for the CB and $\left(d_{x^2} - d_{yx}\right)/2$ for the VB. [41, 42, 43] Due to spin-orbit coupling, the degenerate valleys at the K point split into alternating K^+ and K^- points to which different optical selection rules apply. Each of the valleys interacts only with circularly polarized light of right or left helicity, respectively. However, if linearly polarized light is used, which can be regarded as a linear combination of both helicities, only the energetic splitting is of interest. This is the case in this thesis. Because the splitting of the CB is only a few meV, it can be neglected to a first approximation. However, significant separation of the VB with ~0.4 eV enables the excitation of two transitions in the visible range that are called A and B. [44]

3.2 Excitons in TMDCs

ANALOGOUS to molecules, photons can excite electrons in solids from the VB to the CB, leaving a "hole" in the VB. Due to the attractive Coulomb interaction, they form electron-hole pairs. These quasiparticles are termed excitons. They can move around the crystal and transport their properties (energy, heat, spin, etc.) and dominate the optical properties of TMDCs. [45] There are two limiting approximations for describing an exciton based on the binding energy E_b and the electron-hole radius r_{exc}: Typical inorganic semiconductors possess so-called Wannier-Mott excitons with low binding energies and large electron-hole radii, exceeding the lattice constant a_l. On the other hand, Frenkel excitons are common in organic semiconductors and show high binding energies as well as small radii (figures 3.2a and 3.2b). Interestingly, in TMDC MLs strongly bound electron-hole pairs that extend over several lattice periods are observed. Therefore, they represent an intermediate between the Wannier-Mott and the Frenkel exciton (figure 3.2c). However, the majority of the experimental observations can be appropriately described using the Wannier-Mott picture. [44]

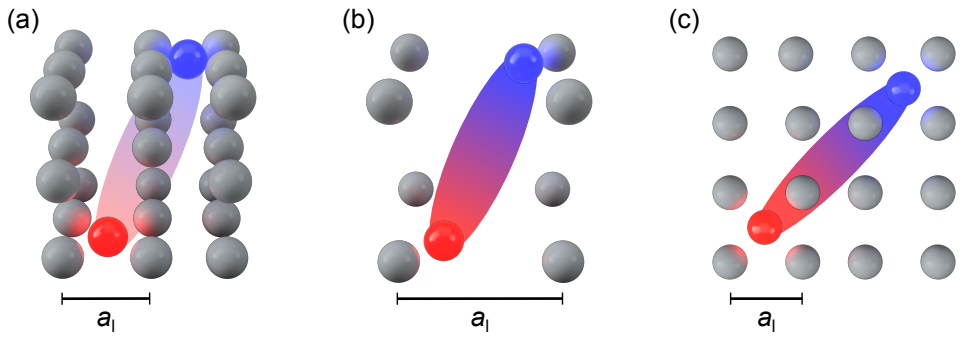

Figure 3.2: Types of excitons. Illustration of (a) Wannier-Mott, (b) Frenkel, and (c) 2D excitons.

The exciton binding energy of Wannier-Mott type excitons can be treated analogously to the hydrogen atom problem. Then, the Hamiltonian $\hat{H}$ reads

$$\hat{H} = -\frac{\hbar\nabla^2}{2\mu} + V_c(r_{exc}), \tag{3.1}$$

where $\hbar$ is the reduced Planck constant, μ is the two-body reduced mass of electron and hole, and $V_c(r_{exc})$ the potential term of Coulomb nature.

Solving the corresponding Schrödinger equation yields the binding energy eigenvalues E_b^n for the 2D case: [46]

$$E_\mathrm{b}^n = \left(\frac{1}{4\pi\varepsilon_0}\right)^2 \frac{\mu e^4}{2\hbar^2 \varepsilon_\mathrm{r} (m-1/2)^2}. \tag{3.2}$$

Here, m is the principal quantum number, e the elementary charge, ε_0 the vacuum permittivity, and ε_r the dielectric constant of the crystal lattice. Generally, the $1s$ exciton state with $n = 1$ is considered to describe the total binding energy of the exciton. Regarding the A exciton, the literature agrees that its exciton binding energy is around 0.5 eV and therefore one order of magnitude larger than in conventional semiconductor materials. However, there is disagreement between the exact values. While some authors report binding energies of ~0.6 to ~0.7 eV [47, 48], others obtain values of ~0.3 to ~0.35 eV. [49, 50]

During radiative recombination, the emission energy E_exc is dictated by the difference between the bandgap energy E_g and the binding energy:

$$E_\mathrm{exc} = E_\mathrm{g} - E_\mathrm{b}^{1s}. \tag{3.3}$$

A consequence of the large binding energies is the very short radiative lifetime of the excitons. In a simple two-band model approach, the radiative lifetime can be written as [14]

$$\mathcal{T}_\mathrm{r} = \frac{\varepsilon}{2\hbar k_0} \left(\frac{E_\mathrm{exc}}{e v_\mathrm{k}} a_\mathrm{B}^\mathrm{2D}\right)^2, \tag{3.4}$$

where

- $\varepsilon = \varepsilon_0 \varepsilon_\mathrm{r}$ is the absolute permittivity,
- $k_0 = E_\mathrm{exc} \sqrt{\varepsilon / (\hbar c)}$ is the light wave-vector and c the speed of light in vacuum,
- $v_\mathrm{k} = \sqrt{E_\mathrm{gap} / (2 m_\mathrm{e})}$ the Kane velocity with the effective electron mass m_e,
- and a_B^2D the 2D exciton Bohr radius.

By approximating with $E_\mathrm{g} \approx 2$ eV, $E_\mathrm{exc} \approx 1.5$ eV ($E_\mathrm{b} \approx 0.5$ eV), $a_\mathrm{B}^\mathrm{exc} \approx 1.5$ nm, and $\varepsilon \approx 1.5\,\mathrm{F \cdot m^{-1}}$, the radiative lifetime of TDMC excitons is estimated to be $\mathcal{T}_\mathrm{r} < 1$ ps [14, 46]. This value is in line with more sophisticated theoretical calculations. [51, 52]

4 CHAPTER

A brief introduction to nonlinear optics

This chapter provides a brief introduction to the essential concepts of nonlinear optics. Basic knowledge of this subject is crucial to understanding the FLUPS setup that was employed in this thesis.

THE fundamental equation of optics, irrespective of whether linear or nonlinear effects are considered, is the wave equation:

$$\nabla \vec{E}(\vec{r},t) - \frac{1}{c^2}\frac{\partial^2 \vec{E}(\vec{r},t)}{\partial t^2} = \mu_0 + \frac{\partial^2 \vec{P}(\vec{r},t)}{\partial t^2}. \tag{4.1}$$

Here, μ_0 is the magnetic permeability of free space, $\vec{E}(\vec{r},t)$ is the electromagnetic pulse field and is $\vec{P}(\vec{r},t)$ the induced optical polarization. For field strengths smaller than 10^9 W/cm^2, the induced polarization is given by

$$\vec{P}(\vec{r},t) = \varepsilon_0 \chi^{(1)} \vec{E}(\vec{r},t)\,. \tag{4.2}$$

Thus, wave equation 4.1 is linear. The tensor $\chi^{(1)}$ is the electric susceptibility and represents a metric for the polarizability of the medium. For a linear wave equation, the superposition principle applies, meaning that incident light rays will penetrate and not influence each other – frequency mixing processes are not possible. To put it in the words of R. Trebinio: "*Life at low intensity is dull.*" [53]

Yet, typical ultrashort pulses reach intensities of $\sim 10^{12}$ W/cm^2 and therefore have electric field strengths comparable to atomic field strengths $E_{at} = e/a_B$, with the Bohr radius of the hydrogen atom a_B. [54] In this case, a nonlinear polarization is induced in the material

that can be described by perturbation theory using a series expansion: [55, 56]

$$\vec{P}(\vec{r},t) = \varepsilon_0 \left[\chi^{(1)} \vec{E}(\vec{r},t) + \chi^{(2)} \vec{E}^2(\vec{r},t) + \chi^{(3)} \vec{E}^3(\vec{r},t) + \ldots \right]. \tag{4.3}$$

Here, $\chi^{(j)}$ is the j-th order susceptibility that mathematically corresponds to a $j+1$-th order tensor, i.e. $\chi^{(1)}$ is a second-order tensor, $\chi^{(2)}$ is a third-order tensor, and so on. The higher-order electromagnetic pulse fields $\vec{E}^2(\vec{r},t)$, $\vec{E}^3(\vec{r},t)$, etc. drive the wave equation 4.1 to yield light at new frequencies. Table 4.1 shows an overview of the optical phenomena that follow from j-th order processes.

Table 4.1: Association of selected optical phenomena to series expansion terms in (4.3).

expansion term	optical phenomena
$\chi^{(1)} \vec{E}(\vec{r},t)$	refraction, absorption, dispersion, birefringence.
$\chi^{(2)} \vec{E}^2(\vec{r},t)$	second-harmonic generation, sum-frequency generation difference frequency generation parametric oscillation.
$\chi^{(3)} \vec{E}^3(\vec{r},t)$	third-harmonic generation, the Kerr effect, two-photon absorption, Raman as well as Rayleigh scattering.

The electric susceptibilities have decreasing coefficients with increasing order, which is why nonlinear fourth-order interactions no longer arise under conventional laboratory conditions. Especially relevant for this work SFG, where two photons of the frequencies ν_1 and ν_2 interact in a nonlinear optical (NLO) crystal to create a new photon of the frequency ν_3. During this process, the photon energy $E = \mathrm{h}\nu$ must be conserved, where h is the Planck constant. In addition, the polarization has a wave vector $\vec{k}$ that must also satisfy momentum conservation: [57]

$$\mathrm{h}\nu_3 = \mathrm{h}\nu_1 + \mathrm{h}\nu_2, \quad \vec{k}_3 = \vec{k}_1 + \vec{k}_2. \tag{4.4}$$

Condition 4.4 is called phase-matching. If not fulfilled, the induced polarization generates new light that is not in phase with the incident light, initiating destructive interference.

Therefore, the upconversion efficiency crucially depends on the phase mismatch $\Delta k = \left|\vec{k}_3 - \left(\vec{k}_1 + \vec{k}_2\right)\right|$, see figure 4.1. The most efficient upconversion will occur at $\Delta k = 0$.

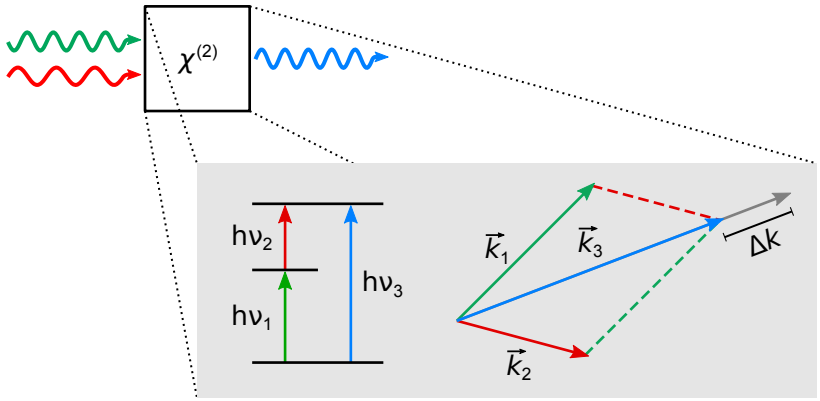

Figure 4.1: Phase-matching in SFG. New, upconverted light is generated in a nonlinear $\chi^{(2)}$-crystal. It is emitted in the direction of wave vector $\vec{k}_3$ and contains the energy of both the fluorescence and the gate.

Experimental part

5 CHAPTER

Fluorescence upconversion spectroscopy

This chapter outlines the experimental details of FLUPS. It begins with a description of the experiment, including the application of SFG for upconversion and the mechanism of temporally resolving the fluorescence response. In the second section, the optical setup is presented and the components, electronics as well as experimental features are explained.

5.1 Basic principles of FLUPS

THE field of nonlinear optics developed rapidly since 1961, shortly after the demonstration of the first laser, and has since then facilitated new applications for time-resolved emission spectroscopy. [58] In 1975, H. Mahr and M. Hirsch were the first to trace the temporal evolution of fluorescence by FLUPS. [59] As shown in figure 5.1a, the sample emission is not directly sent into a detector after excitation, but collected and focused into a NLO crystal. A second pulse, the so-called gate, is also focused on this crystal. When the phase-matching condition is fulfilled (cf. equation 4.4), a new beam, the sum-frequency, is formed:

$$h\nu_u = h\nu_f + h\nu_g, \quad \vec{k}_u = \vec{k}_f + \vec{k}_g. \tag{5.1}$$

The subscripts f, g, and u refer to the fluorescence, gate, and upconverted field. Since the sum-frequency appears at higher frequencies, the signal is referred to as upconverted. In principle, a downconversion can also be contemplated with the appropriate difference-frequency generation (DFG), but this approach is much less established. [60] Generally,

the upconverted signal is measured at individual wavelengths from which the spectra must subsequently be reconstructed. [61] However, by using a suitable NLO crystal and perfectly tuning the crystal properties, angle of incidence, and polarization, broadband detection is achievable. Owing to the inherent advantages over spectral reconstruction, the broadband approach was adopted for this study, details will be discussed in section 6.2.

Note that the mixing of fluorescence and gate exclusively takes place in the presence of both pulses. Therefore, the short-lived gate can sample the comparatively long-lived fluorescence decay at variable time delays τ between pump and probe. The upconverted light reveals information about the sample relaxation as a function of the time delay. Figure 5.1b illustrates that the time resolution Δt is comparable to the pulse width of the gate, i.e. the shorter the pulse, the faster processes can be resolved.

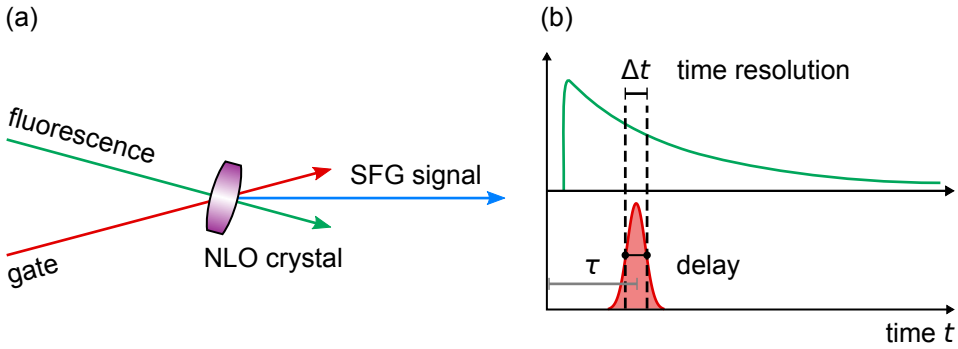

Figure 5.1: Fluorescence upconversion. (a) A segment of the long-lived fluorescence is mixed with the short-lived gate pulse in a NLO crystal. Only a slice of the emission is upconverted; (b) The width of the gate pulse determines the time resolution Δt.

To monitor the fluorescence dynamics, both the gate and fluorescence pulses must not only satisfy phase-matching and spatial overlap, but also temporal overlap. This is because the fluorescence pulse is much more extended in time than the gate pulse. Therefore, the time at which the temporal overlap begins is needed. It is called time zero t_0 and is defined as the time at which the cross-correlation function $C(\tau)$ between the pump and gate pulse is maximal:

$$C(\tau) = \int_{-\infty}^{\infty} I_{\mathrm{g}}(t-\tau)\, I_{\mathrm{pump}}(t)\, \mathrm{d}\tau. \tag{5.2}$$

Both pulses are considered to have a Gaussian line shape. Conceptually, time zero corresponds to the electronic excitation of the sample.

The upconverted signal is also given by a cross-correlation, but in this instance between the fluorescence and the gate pulses. In this case, time zero corresponds to the point in

time where the slope of the sigmoidal signal intensity increase is maximal.

$$C(\tau) = \int_{-\infty}^{\infty} I_g(t-\tau)\, I_f(t)\, d\tau. \tag{5.3}$$

After finding time zero, the experiment is repeated while modifying the time delay between the pump and gate pulses. Figure 5.2 shows that this is realized via incrementally reducing the path length of the pump line by using a motorized translation stage. The move of 0.1 µm corresponds to a change of $t \approx 0.67$ fs in the time domain. Therefore, while the fluorescence pulse arrives at $t = t_0$ in the NLO crystal, the gate arrives with a delay $t = t_0 + \tau$. Accordingly, the decay behavior of the temporally broad fluorescence can be traced. Figure 5.2b illustrates that for each time delay, a transient and upconverted fluorescence spectrum (with an instrumental bias) is collected. When the transient spectra for different delays are evaluated one after another, like a flip-book, information about the time evolution after excitation is gathered.

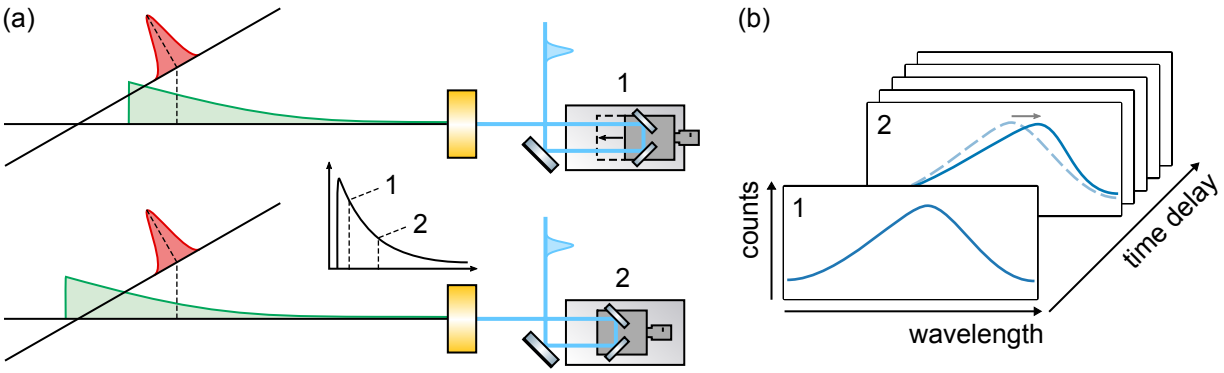

Figure 5.2: Time resolution mechanism. (a) The fluorescence decay can be sampled in the time domain by a variable delay in the pump line; (b) The evolution of transient spectra can be imagined as a series of snapshots at different times.

5.2 Experimental setup

In this thesis, the broadband FLUPS setup established in the laboratory of N. P. Ernsting was adopted. A detailed description of its construction is given in an internal document, the "FLUPS manual". [62] The assembly is based on a titanium-sapphire laser delivering ultra-short, ~1000 µJ pulses with a wavelength of 800 nm at 5 kHz repetition rate.

At first, the fundamental beam is split into two parts, namely the pump and the gate line, using a beam splitter. As discussed, the pump is used to excite the sample, and its fluorescence is then mixed with the gate in a NLO crystal to generate the upconverted signal. A sketch of both beam paths and the employed optics is given in figure 5.3.

The fluorescence (blue beam path) is generated as follows: At first, the pump is frequency-doubled to 400 nm using a NLO crystal and then compressed (not shown). Next, it passes through the variable translation stage T and is then focused on the sample using a lens. For liquid samples, a 1 mm cuvette that is stirred at the focal region by a stream of nitrogen bubbles is employed. After excitation of the sample, the generated PL (green) is collected by the non-axial Schwarzschild objective M1, M2 and focused onto the uniaxial calcite crystal C. As a result of its birefringence, the unpolarized fluorescence is separated into a horizontally and vertically polarized part. Only the vertically polarized PL is collected by the concave mirror M3 and an *ordinary beam* is received. [60] The necessity for this is elaborated in chapter 6.

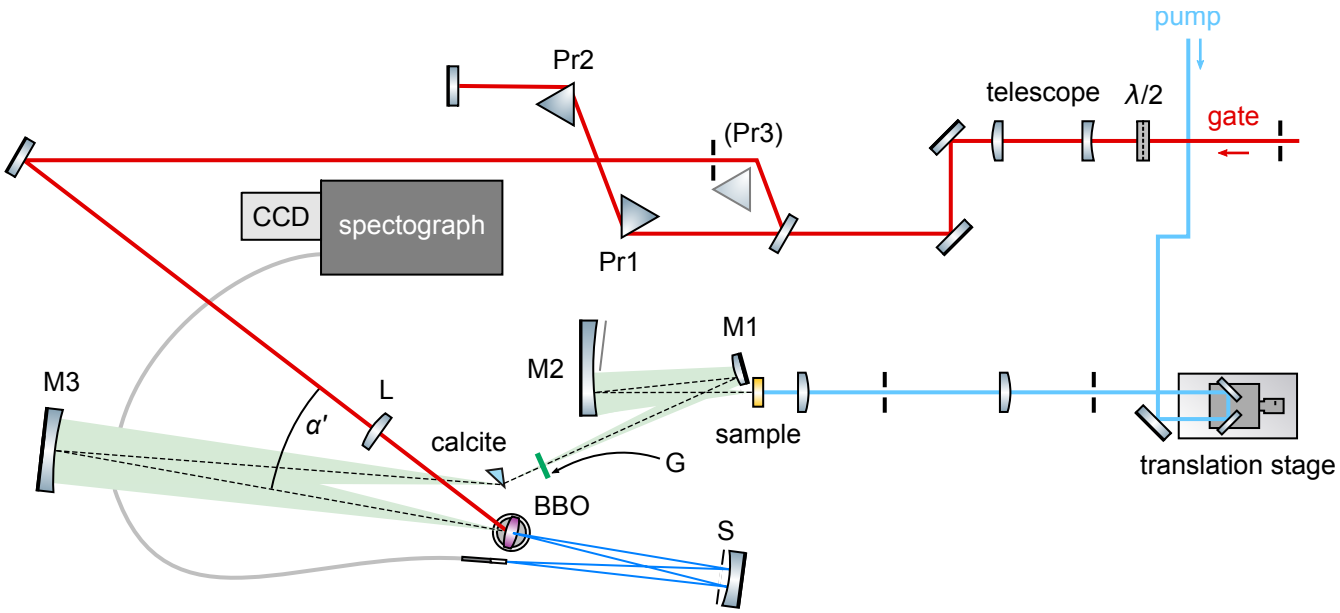

Figure 5.3: Setup of broadband FLUPS. All subsequent measurements of this thesis were conducted with this configuration.

The gate drives a traveling-wave optical parametric amplifier of superfluorescence (TOPAS, not shown) that generates ~200 µJ gate pulses in the near-infrared at 1340 nm (red beam path). Here, the polarization is set to horizontal by a $\lambda/2$ plate so that it becomes an *extraordinary beam* (cf. chapter 6). Then, this beam is expanded as well as collimated by a

telescope and subsequently compressed by the prism compressor Pr1, Pr2. To optimize the spatial overlap between the fluorescence and gate, the size of the latter is reduced using the lens L.

Both the gate and the PL are focused into a NLO crystal. For this experiment, a β-barium borate (BBO) crystal was chosen. In the crystal, both beams coincide with the external interaction angle $\alpha' \approx 22°$. Only if the angle of incidence, polarization, and crystal properties are finely tuned across a broad spectral range, SFG occurs. The presented setup is customized for the upconversion of emission in the range of $425\,\text{nm} \leq \lambda_f \leq 750\,\text{nm}$. To remove background radiation, the pump and non-upconverted fluorescence light are reduced by a Glan filter (bandpass filter) G. It is installed in front of the calcite crystal. [63, 64] Scattered light in the propagation direction is suppressed by the spatial filter W.

Finally, the upconverted signal is focused by a concave mirror to the input of a fiber bundle. The bundle consists of 30 glass fibers with 100 µm diameter. Optical fibers direct the upconverted photons to a grating spectrograph that disperses incoming light onto a rectangular charge-coupled device (CCD) camera with 1600×512 pixels. All columns are connected (full vertical binning); thereby the different signal colors are distributed across the 1600 horizontal pixels. With the described setup, a time resolution of ~400 fs was achieved. A method to receive even better time resolution is described in appendix A11. Data correction and analysis were performed in Python and are described in chapter 7.

Sample preparation and characterization

It is important to prepare samples properly because the spectral traits of dye solutions, as well as solid samples, are sensitive to contaminants. The preparation of the dyes and the TMDC sample was done according to standard procedures.

The desired amount of powdered dye was added to a 4ml tube and the solvent (dehydrated, 99.9% purity) was added. Then, the solution was transferred to a 0.1 mm cuvette and characterized by optical absorption spectroscopy. The optical density OD at the pumping wavelength was determined according to the Beer-Lambert law:

$$\text{OD}_\lambda = \varepsilon(\lambda)\, c d = \lg\left(\frac{I_0(\lambda)}{I(\lambda)}\right). \tag{5.4}$$

Here, c the sample concentration in moles per liter, d the sample thickness, I_0 is the intensity of the incident light, and I is the attenuated intensity.

To reduce the inner filter effect, the solution was diluted if it exceeded $OD_{400\,nm} = 1.5$. This avoids the internal filter effect, cf. section 2.1. In figure 5.4, the absorption spectrum of the considered dye C153 in acetonitrile (cf. result chapters 8 and 9) is depicted.

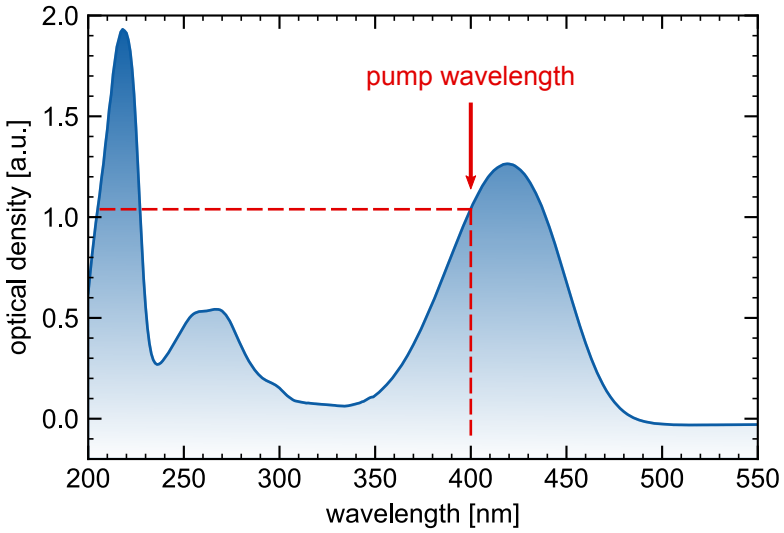

Figure 5.4: Absorption spectrum of C153. The optical density at 400 nm is highlighted.

Tungsten disulfide (WS_2) was chosen as the 2D solid sample for further investigations because it has the highest quantum yield of the group IV TMDCs. X. Zhu's group produced high-quality WS_2 pristine MLs by gold-assisted mechanical exfoliation of CVD grown crystals. The WS_2 flakes were deposited on a silicon substrate coated with a thin silicon oxide layer (Si/SiO_2 substrate). Synthesis details are outlined in references [65] and [66], respectively. The MLs were characterized using optical microscopy; images will be discussed in chapter 10. Due to contact with airborne contaminants, the sample was regularly cleaned using blasts of compressed air.

6 CHAPTER

Phase-matching considerations

The chapter outlines the various peculiarities concerning phase-matching in FLUPS, with broadband detection being the major challenge. The first section lays out the properties of the NLO crystal and its effect on the polarization of the outgoing light. The distinctive strategies for broadband phase-matching are presented and the one that was realized in this work is discussed. Finally, the two modes in which the setup can be run are introduced and their specific attributes elaborated.

6.1 Properties of the NLO crystal

THE choice of the nonlinear material, as well as the properties of the incident beams, are of paramount importance for effective SFG. A major difficulty in FLUPS is to find suitable phase-matching conditions that satisfy equation 5.1. This section presents the principles and design decisions to achieve phase-matching in FLUPS, which have already been addressed in the listed reviews: [67, 68, 69].

As discussed, phase-matching takes place in a NLO crystal. In optical applications, these are usually anisotropic, which becomes apparent when reconsidering equation 4.3. For crystals with inversion symmetry, special inversion $\vec{r} \rightarrow -\vec{r}$ implies both $E(-\vec{r}) = -E(\vec{r})$ and $P(-\vec{r}) = -P(\vec{r})$. To satisfy the latter, even orders of electrical susceptibility must vanish.

For anisotropic crystals, light can behave differently depending on its polarization, which is also true for linear processes. This effect is called birefringence. In the linear regime, the

electric susceptibility $\chi^{(1)}$ can be written in matrix form as

$$\underline{\chi}^{(1)} = \begin{pmatrix} \chi_{11} & \chi_{12} & \chi_{13} \\ \chi_{21} & \chi_{22} & \chi_{32} \\ \chi_{31} & \chi_{32} & \chi_{33} \end{pmatrix}. \tag{6.1}$$

When a non-magnetic and transparent crystal is present, $\underline{\chi}^{(1)}$ is symmetric and its elements are real. [70] It is known from linear algebra that real and symmetric matrices are diagonalizable so that a coordinate system can be found in which $\underline{\chi}^{(1)}$ reads

$$\underline{\chi}^{(1)} = \begin{pmatrix} \chi_x & 0 & 0 \\ 0 & \chi_y & 0 \\ 0 & 0 & \chi_z \end{pmatrix}. \tag{6.2}$$

The diagonal elements χ_x, χ_y, and χ_z are the principal dielectric axes and can be expressed as refractive indices, respectively:

$$n_j = \sqrt{\chi_j + 1}, \quad j = x, y, z. \tag{6.3}$$

For the following thoughts, it is convenient to investigate the analog matrix $\underline{n}$ instead of $\underline{\chi}^{(1)}$:

$$\underline{n} = \begin{pmatrix} n_x & 0 & 0 \\ 0 & n_y & 0 \\ 0 & 0 & n_z \end{pmatrix}. \tag{6.4}$$

Consider a crystal that is not isotropic but still retains some symmetry. Then, two of the refractive indices can be equal, e.g. $n_x = n_y \neq n_z$. This type of birefringence was applied in this thesis and is termed uniaxial. The direction in which each polarization component does not experience birefringence is the optic axis. The incident light beam and the optic axis are spanning a plane. If a beam is polarized perpendicular to this plane, it is called ordinary (o) and refracted with n_o. On the other hand, if the polarization lies in this plane, it is an extraordinarily (e) beam with a refractive index n_e. Typical nonlinear birefringent crystals like BBO and potassium dideuterium phosphate (KDP) are negatively uniaxial, i.e. $n_\mathrm{e} < n_\mathrm{o}$. [71, 72] While n_o is independent of the beam propagation, n_e is a function of the phase-matching angle θ between the optic axis and the incident beam. They obey the following relationship: [73]

$$n_\mathrm{e}(\theta) = n_\mathrm{o} \sqrt{\frac{1 + \tan^2\theta}{1 + (n_\mathrm{o}/n_\mathrm{e}) \tan^2\theta}}. \tag{6.5}$$

The different refraction indexes can be depicted as an index ellipsoid, see figure 6.1.

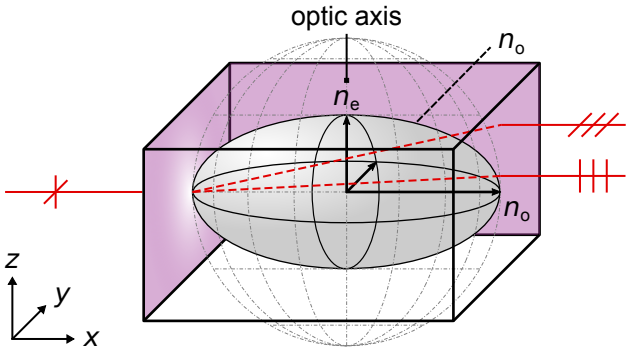

Figure 6.1: Index ellipsoid. A beam of light enters along the x-direction into a negative uniaxial crystal. The unpolarized beam can be deconstructed into polarizations in the xz- and xy-plane. They experience the refraction n_e and n_o, respectively. The optic axis is along the z-axis, such that the light polarized in the xz-plane is refracted less (with $n_e < n_o$).

In addition, n_o and n_e are also wavelength dependent. They can be empirically described by the Sellmaier equations. For a BBO crystal, these have the following form (λ in µm): [74, 75]

$$n_o^2(\lambda) = 2.7359 + \frac{0.01878}{\lambda^2 - 0.01822} - 0.01354\,\lambda^2, \tag{6.6}$$

$$n_e^2(\lambda) = 2.3753 + \frac{0.01224}{\lambda^2 - 0.0166} - 0.01516\,\lambda^2. \tag{6.7}$$

6.2 Broadband phase-matching

Because of technical considerations that are discussed at the end of this chapter, the fluorescence polarization was set to ordinary and the gate polarization to extraordinary, cf. section 5.2. Considering equations 4.4, 6.5, 6.6, and 6.7 for the collinear case, the phase-matching condition as well as the mismatch can be written in terms of refractive indices:

$$\frac{n_o(\lambda_f)}{\lambda_f} + \frac{n_e(\theta)}{\lambda_g} = \frac{n_o(\lambda_u, \theta)}{\lambda_u}, \tag{6.8}$$

$$\Delta k = \frac{n_o(\lambda_u, \theta)}{\lambda_u} - \left(\frac{n_o(\lambda_f)}{\lambda_f} + \frac{n_e(\theta)}{\lambda_g} \right). \tag{6.9}$$

Because λ_g is, at least in the first approximation, a number, the refractive index n_e is wavelength-independent. In contrast, λ_f is an interval. As mentioned in chapter 4, the

mixing process is optimal if $\Delta k = 0$. However, this is only the case for a single wavelength which is determined by a corresponding phase-matching angle. Because of strict phase-matching, mostly a narrow band of wavelengths centered around $\lambda_{\mathrm{f}}^{(\theta)}$ is upconverted, as for example in the selected references [76, 77, 78, 79]. Because the spectral evolution of the PL contains ancillary information about the researched process, M. Maroncelli *et al.* collected intensity traces $I_{\mathrm{u}}(\tau)$ at different wavelengths by varying the phase-matching angle. Then, they reconstructed the fluorescence spectrum. [80, 81] However, due to better photometric accuracy, it is desirable to have a continuous emission spectrum for any delay time.

Already in 1983, Barbara *et al.* succeeded in performing broadband fluorescence upconversion with a spectral width of 75 nm. [82] Since then, efforts have been undertaken by several research groups to cover the entire emission range of the fluorophore. This has been realized in different ways:

(i) T. Gustavson *et al.* rotated the NLO crystal at a constant velocity to realize phase-matching for the entire spectral range. At the same time, they recorded the signal by scanning the monochromator simultaneously with rotation. [83, 84]

(ii) Research groups led by S. Haacke and M. Chergui also rotated the NLO crystal at a constant speed but detected the signal in a spectrograph. [85, 86]

(iii) N. P. Ernsting *et al.* achieved concurrent phase-matching over a wide spectral range without modifying the phase-matching angle. [87, 73]

Although implementations (i) and (ii) benefit from a less complicated experimental setup, crystal rotation might introduce geometric instabilities that can affect measurement accuracy. Therefore, the “silver bullet” is method (iii), which benefits from superior background suppression, signal-to-noise ratio (SNR), and a fixed geometry.

Therefore, method (iii) was chosen for this work. It is based on tolerance phase-matching. Although the phase-matching conditions are not precisely met for all λ_{f}, energies with a small deviation from perfect phase-matching are still upconverted. The upconversion efficiency falls with increasing phase mismatch as [61]

$$\eta(\Delta k) = \text{const.}\, I_{\mathrm{g}} L^2 \frac{\sin^2(\Delta k L)}{(\Delta k L)^2}. \tag{6.10}$$

The constant in the equation above is determined by the properties of the incident fluorescence and gate radiation as well as by the susceptibility coefficients of the NLO crystal. Equation 6.10 also shows that the upconversion efficiency can be improved by increasing the gate pulse intensity I_g or crystal thickness L. A high gate intensity does not carry any disadvantages; the limiting factor for increasing it is the damage threshold of the NLO crystal. However, there is a disadvantage in raising the crystal thickness: The spectral coverage decreases at the same time, cf. figure 6.2. Therefore, to retrieve a broad spectral bandwidth, the crystal thickness should be decreased. Qualitatively, a decline in upconversion efficiency with decreasing crystal thickness according to equation 6.10 was noticed experimentally. However, a dramatic scaling with L^2 has not been recognized. Depending on the attributes of sample emission, certain compromises must be made in choosing the NLO crystal, both in material and thickness.

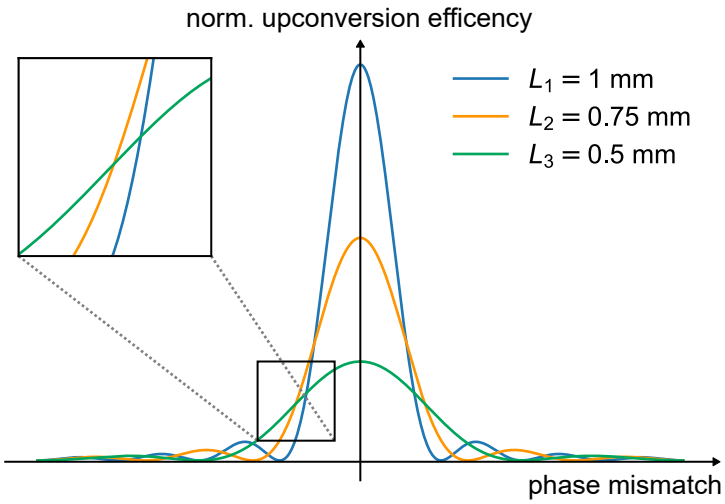

Figure 6.2: Upconversion efficiency. The figure displays a comparison of the upconversion efficiency for different crystal thicknesses: A large thickness (blue) possesses comprehensive maxima, but they descent quickly for a rising phase mismatch. A reverse trend can be seen for smaller L (green).

Type I and II phase-matching

Inherently, upconversion is a polarization-selective process. In general, phase-matching conditions cannot be satisfied if all three f, g, and u waves propagate as ordinary rays in the crystal. However, if one or more of the rays propagate as extraordinary rays, the phase-matching conditions can be satisfied.

Therefore, depending on the polarization of the two input fields, two types of phase-matching are distinguished for negative uniaxial crystals:

- Type I: o + o → e
  Two ordinary beams are mixed, resulting in an extraordinary beam. Here, the experimental FLUPS geometry is comparatively simple and has higher efficiency, but is also more strict compared to type II phase-matching. Therefore, type I is mostly used for monochromatic upconversion implementations. The optimal phase-matching angle for type I can be solved analytically.
- Type II: e + o → e
  In this phase-matching type, an ordinary and an extraordinary input produce an extraordinary signal wave. This constellation allows phase-matching over a wider frequency range compared to type I and is thus used in this work. The optimal phase-matching angle for type II must be determined numerically.

In conclusion, broadband tolerance phase-matching of type II represents the superior, but also the most ambitious approach to upconvert fluorophore emission. The appropriate NLO crystal and optimal geometrical conditions for such a spectrometer have been scrutinized and fine-tuned for over 20 years in the group of N. P. Ernsting.

6.3 Measurement modes

UNTIL now, only an adjustment of the phase-matching angle was evaluated. This allows selecting the central wavelength[1] around which tolerance phase-matching is performed. However, in addition to a fixed phase-matching angle, the orientations of the crystal φ must also be optimized. This is done by rotating around the surface normal.

M. Gerecke *et al.* showed in a novel publication that two crystal orientations φ exist for which effective upconversion occurs. [88] These two different phase-matching configurations correspond to two measurement modes that the authors termed *case A* and *case B*. They also addressed how to identify these two local optima.

Besides upconversion, other nonlinear processes can also arise in the BBO, for instance second-harmonic generation (SHG) or third-harmonic generation (THG) of the gate. The

[1] The central wavelength is the wavelength of maximum emission.

scattered light of the second harmonic is visible (~670 nm) and its intensity is proportional I_g^2. If one of the two optimal crystal orientations is approached during rotation, the intensity of scattered gate light passes through a minimum as the gate intensity depletes due to upconversion. How the minimum is reached is unique for the measurement modes. In case A, the minimum is very sharp, while the scattered gate light is bright close to the minimum. By contrast, case B shows a broad minimum and low second-harmonic gate intensity for slight angular discrepancy.

Now the question arises of how the two measuring modes are distinct from each other. Experimentally, the following is found:

Case A is characterized by a superior efficiency with a factor of three to five, while case B has a wider phase-matching bandwidth.

To elucidate the differences in efficiency between the measurement modes, M. Gerecke *et al.* additionally inspected their phase-matching behavior [88]. Their results are summarized in figure 6.3. The upper channel (figure 6.3a) presents the interaction geometry in cases A and B. In both instances, the fluorescence and gate pulses encounter the BBO with the external interaction angle

$$\alpha' = \delta'_f - \delta'_g. \tag{6.11}$$

Here, δ' is the external incidence angle of the pulse with respect to the surface normal. By Snellius' law of refraction, the external angles are transformed to internal angles when they encounter the BBO:

$$\sin\delta'_f = n_o(\lambda_f)\sin\delta_f, \tag{6.12}$$

$$\sin\delta'_g = n_e(\lambda_g,\theta)\sin\delta_g. \tag{6.13}$$

The z-axis of the internal coordinate system is along the optic axis and is considered to be positive in the direction of the escaping beams. The wave vectors of the fluorescence, gate, and upconverted signal span internal angles θ_f, θ_g, and θ_u with the optic axis.

The authors confirmed numerically that for the interaction geometry displayed in the schematic, the dispersion in phase-mismatch $\Delta k = \left|\vec{k}_u - \left(\vec{k}_f + \vec{k}_g\right)\right|$ is pronounced for case A. Consequently, small deviations from perfect phase-matching promptly display a lower efficiency. In contrast, case B exhibits a significantly lower dispersion and therefore holds larger spectral coverage.

To understand the discrepancy in efficiency, figure 6.3b is considered. It presents the differences in phase-matching between the two cases. Both the internal angles and the corresponding wave vectors are depicted on polar graphs. The dashed gray line indicates perfect phase-matching. It becomes apparent that θ_g and θ_u are smaller in case A than in case B. This allows distinguishing their phase-matching behavior. Due to angular dispersion, the fluorescence light is focused in the shape of a cone into the BBO. Consequently, there also exist fluorescence vectors (green) with detuned internal angles θ_f. They lie on a circle apart from the central angle θ_f^c. The zoom into the circle's intersection demonstrates that detuned upconversion vectors (blue) lie in proximity to the optimal solution in case A. However, tolerance phase-matching is quickly lost in case B. This means that case A holds higher angular acceptance of the incident fluorescence radiation, i.e. more photons of the fluorescence cone are upconverted. This explains the superior efficiency in case A.

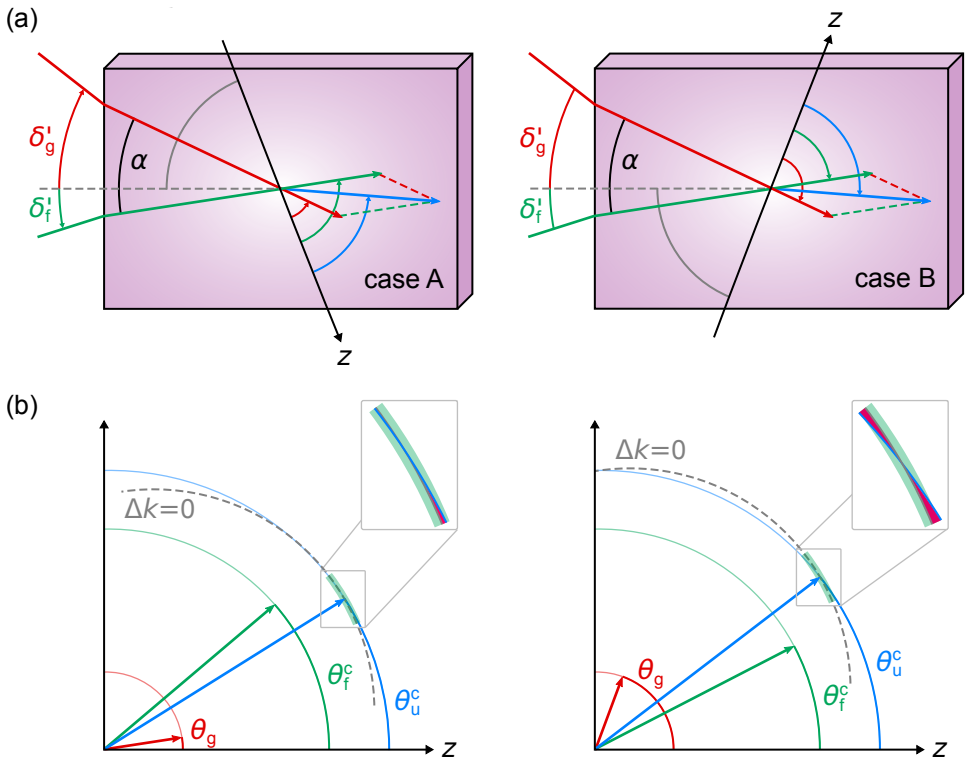

Figure 6.3: Theoretical comparison of cases A and B. (a) Interaction geometry in cases A and B. They can be distinguished by the order in which the wave vectors form internal angles with the optic axis; (b) Wave vector components in a polar representation. Different internal angles for cases A and B yield distinctive phase-matching features. The purple shading in the boxes highlights the departure from perfect phase-matching. The figure is adopted from reference [88].

7 CHAPTER

Photometric Correction

This chapter introduces the photometric correction that is a necessary step in data analysis to address the instrumental bias. Photometric correction is especially important for CCD detection systems because the sensitivity of these devices is typically wavelength-dependent. The focus is on the mathematical principles of the correction procedure, experimental results are presented in the next chapter.

As mentioned in section 5.2, the upconverted signal is a count distribution s as a function of pixels p at the CCD camera

$$s(p) = \frac{\partial \sigma}{\partial p}, \tag{7.1}$$

where σ is the total number of signal counts. Each pixel corresponds to a wavelength according to the following relationship:

$$\lambda_u = 0.122 \cdot p + 303.047. \tag{7.2}$$

However, the transient count distribution gathered at the detector does not correspond to the "true" upconverted fluorescence spectrum f. [89] The main reason for this is the wavelength-dependence of the upconversion process, cf. equation 6.10. This bias is mathematically captured by the instrument response function (IRF) :

$$s(\lambda_u) = f(\lambda_u) \cdot \mathrm{IRF}(\lambda_u). \tag{7.3}$$

Figure 7.1 exemplifies how the IRF can distort the detected photon distribution.

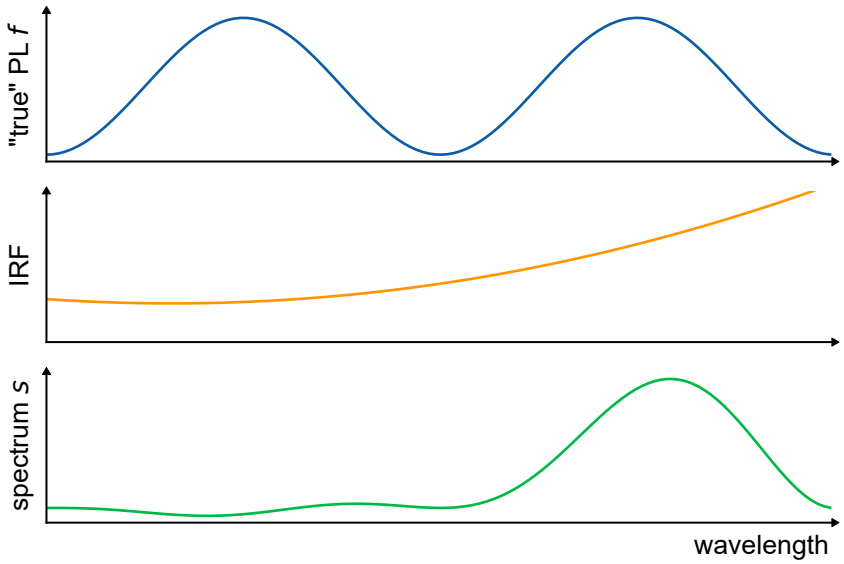

Figure 7.1: Instrument response function. The "true" fluorescence spectrum f (blue) is distorted by the IRF (orange) during acquisition, resulting in the measured spectrum s (green).

That is why the measured spectrum $s(\lambda_u)$ must be photometrically corrected. A correction function $c(\lambda_u) \propto \mathrm{IRF}^{-1}(\lambda_u)$ is sought which yields the legitimate upconverted fluorescence spectrum $f(\lambda_u)$ upon pointwise multiplication:

$$f(\lambda_u) \propto c(\lambda_u) \cdot s(\lambda_u). \tag{7.4}$$

How can $c(\lambda_u)$ be obtained? The method described by N. P. Ernsting's group in 2011 was adopted for this purpose [32]: Consider a FLUPS experiment with a standard dye such as C153. The fluorescence spectrum $f(\tilde{\nu}_f)$ can be calculated *in silico* as a sum of four-parametric lognormal functions

$$f(\tilde{\nu}_f) = \sum_{j=1} \mathrm{logn}_j(\tilde{\nu}_f) \tag{7.5}$$

with

$$\mathrm{logn}_j(\tilde{\nu}_f) = a_j \exp\left(-\ln 2 \left\{ \frac{\gamma_j \ln\left[1 + 2\gamma_j\left(\tilde{\nu}_f - \tilde{\nu}_{0,j}\right)\Delta_j^{-1}\right]}{\gamma_j} \right\}^2\right). \tag{7.6}$$

Here, a is the amplitude, $\tilde{\nu}_0$ the peak wavenumber, Δ the bandwidth, and γ the asymmetry. As an example, the fitting parameters for C153 in acetonitrile are summarized in table 7.1. [88] For further calculations, $f(\tilde{\nu}_f)$ was normalized.

Table 7.1: Lognormal parameters from equation 7.6 for C153 in acetonitrile. Only two lognormal functions are required.

amplitude a	peak wavenumber $\tilde{\nu}_0$ [cm^{-1}]	bandwidth Δ [cm^{-1}]	asymmetry γ
0.9333	18803	3287	−0.2771
0.1206	19589	1339	−0.0760

Next, the fluorescence photons are transformed into an equivalent distribution of upconverted photons with $\tilde{\nu}_\mathrm{u} = \tilde{\nu}_\mathrm{f} + \tilde{\nu}_\mathrm{g}$. To compare the calculated spectrum with the experimental one, the former is converted into units of wavelength or pixels, respectively. From conservation of energy follows: [90, 91]

$$f(\lambda_\mathrm{u})\,\mathrm{d}\lambda_\mathrm{u} = f(\tilde{\nu}_\mathrm{u})\,\mathrm{d}\tilde{\nu}_\mathrm{u}, \tag{7.7}$$

$$\Leftrightarrow f(\lambda_\mathrm{u}) = f(\tilde{\nu}_\mathrm{u})\frac{\partial\tilde{\nu}_\mathrm{u}}{\partial\lambda_\mathrm{u}} = f(\tilde{\nu}_\mathrm{u})\,\lambda_\mathrm{u}^{-2}. \tag{7.8}$$

Now the correction function can be derived using equation 7.4. Finally, a polynomial fit provides the smooth correction function $\bar{c}(\lambda_\mathrm{u})$.

For initial measurements in chapter 8, C153 is the sample under investigation. However, there are fluorophores or materials where the emission spectrum cannot be obtained *in silico*. Then, an appropriate standard dye solution must be prepared for which the stationary distribution can be calculated as described in this chapter. This dye solution must cover the entire spectral range of the sample emission. If the emission is broad, the spectral range can be covered by combining several standard dye solutions.

Results

8 CHAPTER

Characterization of the setup

This chapter presents FLUPS measurements of C153 in acetonitrile. First, steady-state spectral features of the system are discussed. Then, upconversion of the fluorescence is performed and it is shown that the photometric correction is necessary to retrieve the legitimate emission spectra. Furthermore, the high stability of the correction is verified. The second section describes the solvation dynamics of C153, revealing a distinctive TDSS. The transient spectra are fitted and the spectral evolution is quantified, showing satisfactory agreement with the literature.

8.1 Spectroscopy of C153 in acetonitrile

Because FLUPS is a highly sensitive experiment with various sources of error, its performance must first be confirmed before unknown systems can be investigated. Therefore, first measurements with C153 in the polar solvent acetonitrile were performed. If the FLUPS setup operates, then the TDSS of C153 assessed in the literature should be detected. For the subsequent investigations, a solution of C153 in acetonitrile was prepared with an optical density $OD_{400\,nm} \approx 1.0$.

Steady-state spectroscopy

The steady-state absorption and fluorescence spectra of C153 in acetonitrile are shown in figure 8.1. In polar solvents, the peaks are fairly featureless as the vibrionic structure is lost. [29] The spectral characteristics of C153 perfectly match the experimental design

of the setup: The local absorption peak (purple) is close to 400 nm and therefore C153 absorbs a large part of the pump energy. In addition, the emission (green) is between 450 nm and 670 nm and thereby within the wavelength range of 425 nm to 750 nm that can be efficiently upconverted. Consequently, C153 is ideally suited to characterize the functionality of the implemented FLUPS.

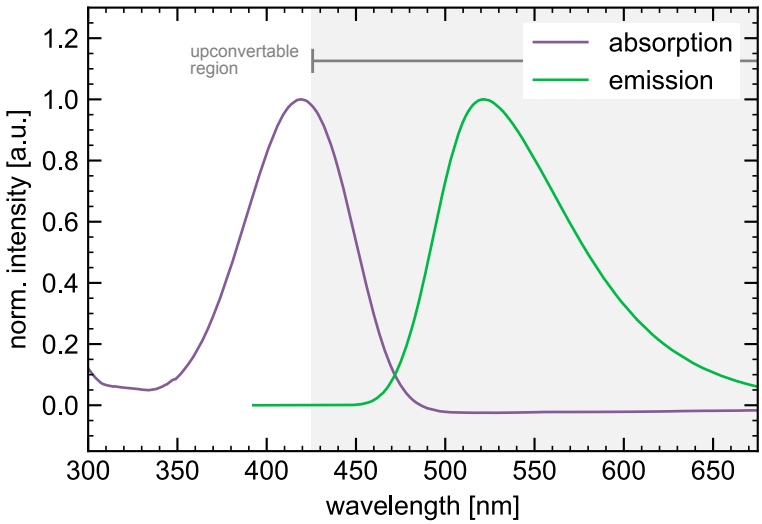

Figure 8.1: Absorption and emission of C153 in acetonitrile. The steady-state spectra behave like image and mirror image. The emission range covered by FLUPS is shaded in gray.

Time-resolved spectroscopy

To perform the upconversion, ~400 nJ pump and ~200 µJ gate pulses were used. Then, transient spectra from −2 up to 10 ps around $t_0 := 0$ fs were recorded in 50 fs steps. Throughout the experiments, the exposure time of the CCD camera has been 1 s.

Raw upconversion spectra are recorded as a function of horizontal CCD pixel or wavenumber with an instrumental bias. To rectify the bias, the photometric correction is performed as outlined in chapter 7. Figure 8.2 displays the four major steps of the procedure. First, the unbiased spectrum is generated *in silico* (figure 8.2a). The corresponding fitting data are given as a function of wavenumbers, cf. table 7.1. After the transition to a wavelength scale, the calculated spectrum is upconverted (figure 8.2b). Then, the upconverted fluorescence spectra are included as a function of wavelength. A comparison of the unbiased spectrum (orange) and the experimental one (blue) shows a clear deviation of the peak position and

shape (figure 8.2c). This is why inaccurate results are retrieved without performing the photometric correction. Finally, the correction function can be derived (figure 8.2d). All transient spectra are multiplied with this function.

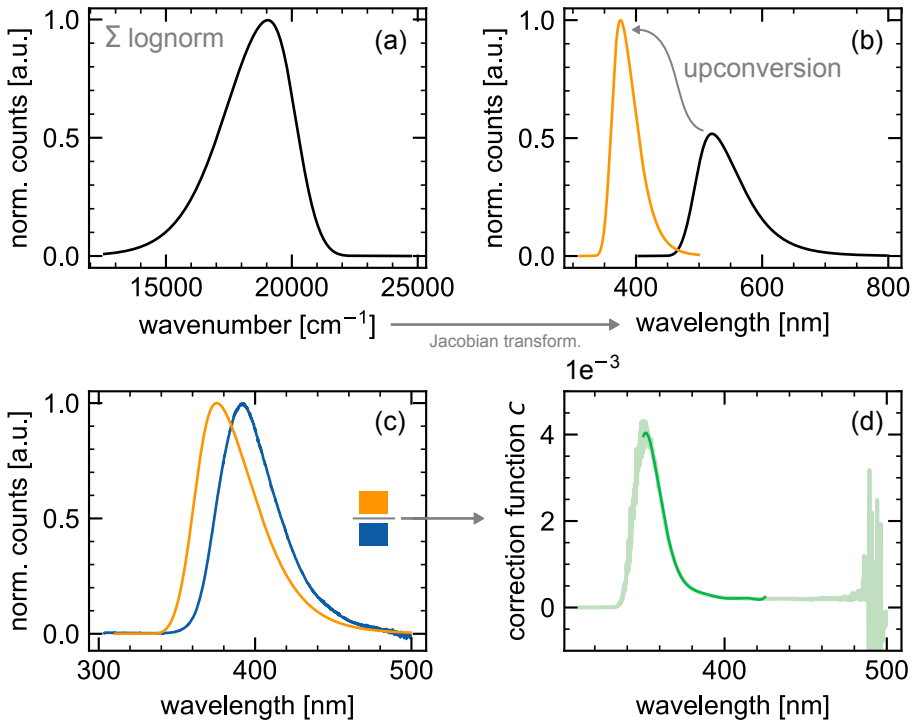

Figure 8.2: Photometric correction I. First, the fluorescence response of the sample is described by a sum of lognormal functions using a wavenumber scale (black). Next, the count distribution is upconverted (orange) and compared to the count distribution that carries an instrumental bias. The correction function (green) eliminates this bias upon multiplication with the collected spectra.

A comparison of the transient and photometrically corrected spectra is given in figure 8.3: The left panel shows the temporal evolution of the spectra before photometric correction, the right graph afterward. The color bar indicates the normalized count values, where blue corresponds to positive and red to negative count values. The negative values are due to the background correction and intensity fluctuations of the gate. It becomes evident that the photometric correction leads to a significant blue shift of the upconverted spectra. This reveals the inferior FLUPS performance on the "blue side". While the uncorrected traces do not reveal a notable peak shift, a distinct redshift in the first picosecond can be witnessed for the corrected measurement.

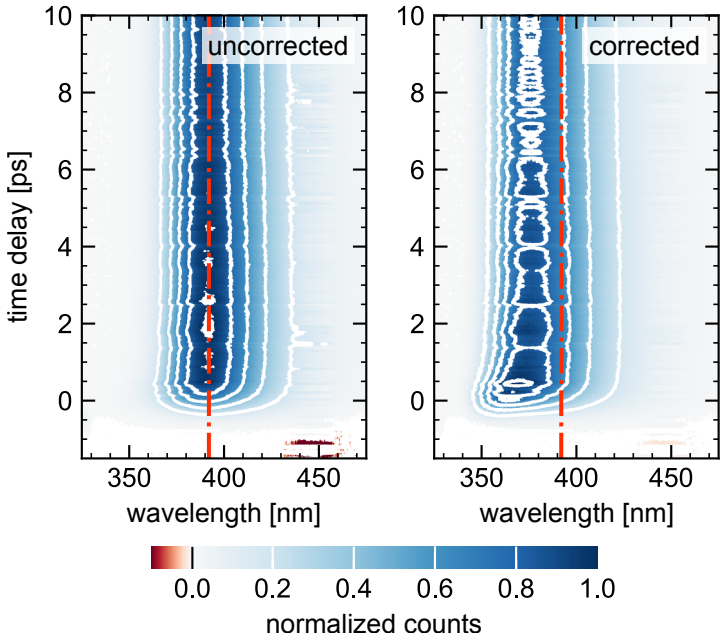

Figure 8.3: Photometric Correction II. Upconverted fluorescence spectra of C153 in acetonitrile as a function of time delay. On the left are raw and on the right photometrically corrected spectra. The red dashed line illustrates the emission peak of the uncorrected spectra that is approximately constant in time.

As discussed, the objective of the photometric correction is to retrieve the unbiased upconverted fluorescence spectra $f(\lambda_u)$. As a consequence, they should only be dependent on the sample and independent of the IRF. To verify this, the phase-matching angle and thus the IRF was changed and the corresponding transients $s(\lambda_u)$ were detected. In figure 8.3, optimal phase-matching was applied. Here, the optimal phase-matching angle θ_{opt} is defined by a maximum peak height of $s(\lambda_u)$. If the photometric correction fulfills its purpose, then the corrected spectra must be similar for different angles $\theta_{opt} \pm \Delta\theta$ as long as $\Delta\theta$ is small. Figure 8.4 summarizes the results: In the upper panel, it becomes apparent that the time evolution of the uncorrected spectra $s(\lambda_u)$ differs for particular phase-matching angles, as anticipated. The lower panel depicts the photometrically corrected traces $f(\lambda_u)$. These are almost identical (except for the intensity) which confirms the high stability of the procedure.

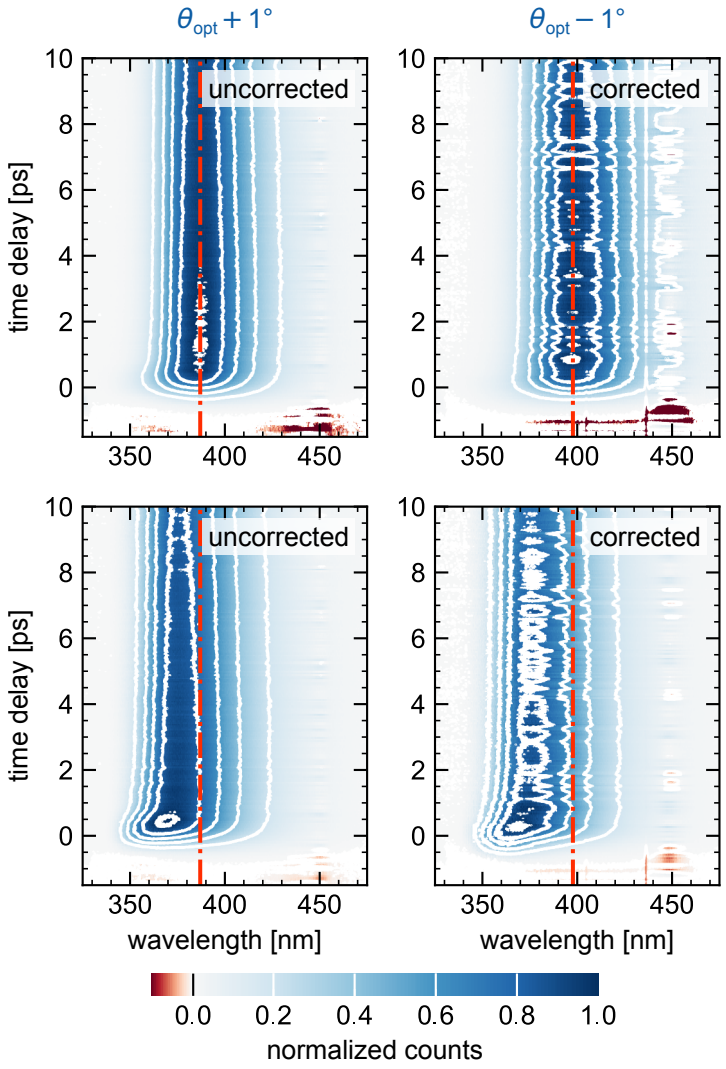

Figure 8.4: Photometric Correction III. Upconverted fluorescence spectra of C153 in acetonitrile are depicted as a function of time delay. The upper panel shows the raw evolution with one degree increase or decrease of the phase-matching angle. The lower panel shows the photometrically corrected spectra from the top. Again, the red dashed lines mark the emission peak of the uncorrected spectra.

8.2 Femtosecond dynamics of C153

TRANSIENT, photometrically corrected fluorescence spectra at several delay times between the threshold t_0 and t_∞ spectra are given in figure 8.5. Here, the steady-state t_∞ spectrum corresponds to the long-term average emission spectrum which is also accessi-

ble by conventional fluorescence spectroscopy. Because the sampling of 50 fs is higher than a time resolution of ~400 fs, the transient spectra are averaged using three traces around the specified time delay in the legend. The t_∞ spectrum was obtained by averaging transient spectra from 8 to 10 ps. This is reasonable because the emission peak is reported to transition to the steady-state state within ~6 ps after excitation. [32] The intensity of the transient spectra is normalized to the steady-state intensity. Note that the following spectra are plotted at upconverted (lower) wavelengths. In the literature, these are sometimes presented without the energy of the gate, i.e. at their natural emission wavelength.

Particularly noticeable in figure 8.5 is a distinct, time-dependent redshift of the transient spectra. It occurs at an ultrafast timescale that is nearly complete after 1 ps. Furthermore, a modification of the spectral intensity and shape, e.g., width and asymmetry, can be detected during the early time evolution.

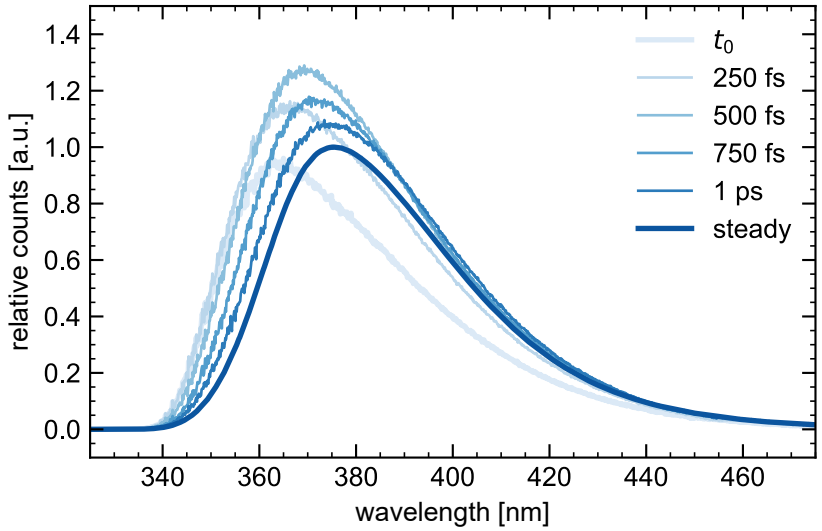

Figure 8.5: FLUPS spectra of C153. Evolution of the upconverted and photometrically corrected fluorescence spectra of C153 in acetonitrile at selected time delays.

To quantify the spectral response, each transient spectrum was fitted with a single four-parameter lognormal distribution according to equation 7.6. Therefore, the lineshape is defined by the peak wavenumber $\tilde{\nu}_0$, the bandwidth Δ, and the asymmetry parameter γ. Siano and Metzler empirically confirmed that these functions are a good analytical description of smooth absorption [92]. Later, studies showed that this approach can be generalized to emission. However, the lognormal approximation of the fluorescence spectra is typically used as a convenient analytical description. Whether it contains any physical meaning is generally not revealed. [93]

The development of the four parameters within the first 10 ps is depicted in figure 8.6 (next page).

Figure 8.6a reveals the rapid evolution of the peak wave number, which proceeds on a timescale of < 100 fs. Therefore, the dynamics cannot be fully resolved with the available time resolution. The width parameter from figure 8.6b reveals peak narrowing after excitation that occurs on a much smaller timescale. Figure 8.6c depicts a rapid decrease of the asymmetry parameter, analogous to the peak shift.

Overall, the evolution of the parameters in figure 8.6 exhibits at least biexponential behavior with two components: An ultrafast component with < 2 ps and a slower component of the order of tens of picoseconds. The ultrafast component can be attributed to the solvation dynamics and represents a TDSS. This dynamical peak shift corresponds to the rapid redshift from figure 8.6a. Interestingly, the dynamics of the asymmetry parameter seem to follow that of the peak shift, but the reason for this behavior is unclear. [73] The evolution of the width parameter contains the larger time component that can be rationalized by cooling dynamics. Most likely, the decay is due to the thermalization of vibrations. [94, 95]

Figures 8.6b and 8.6c demonstrate that the transient spectra become narrower and slightly more symmetric with increasing time delay. These observations are also in agreement with the literature. [73]

For a numerical comparison, the TDSS is an excellent benchmark. It is calculated from the threshold spectra using $\tilde{\nu}_0(t_0) - \tilde{\nu}_0(t_\infty)$ and amounts to ~1600 cm^{-1}. This value also agrees well with the value of ~1700 cm^{-1} obtained by N. P. Ernsting's group. [73] The discrepancy can be explained by their higher time resolution. They accomplished it by implementing a pulse tilt of the gate; their proceeding is discussed in the appendix A11.

The averaging of initial shifts in the present work likely leads to a slight underestimation of the TDSS. This hypothesis is consistent with the results of Maroncelli *et al.* who acquired a shift of ~1450 cm^{-1} with an inferior time resolution of ~500 fs.[1] [96]

[1] Note that no FLUPS, but a Kerr shutter setup was employed.

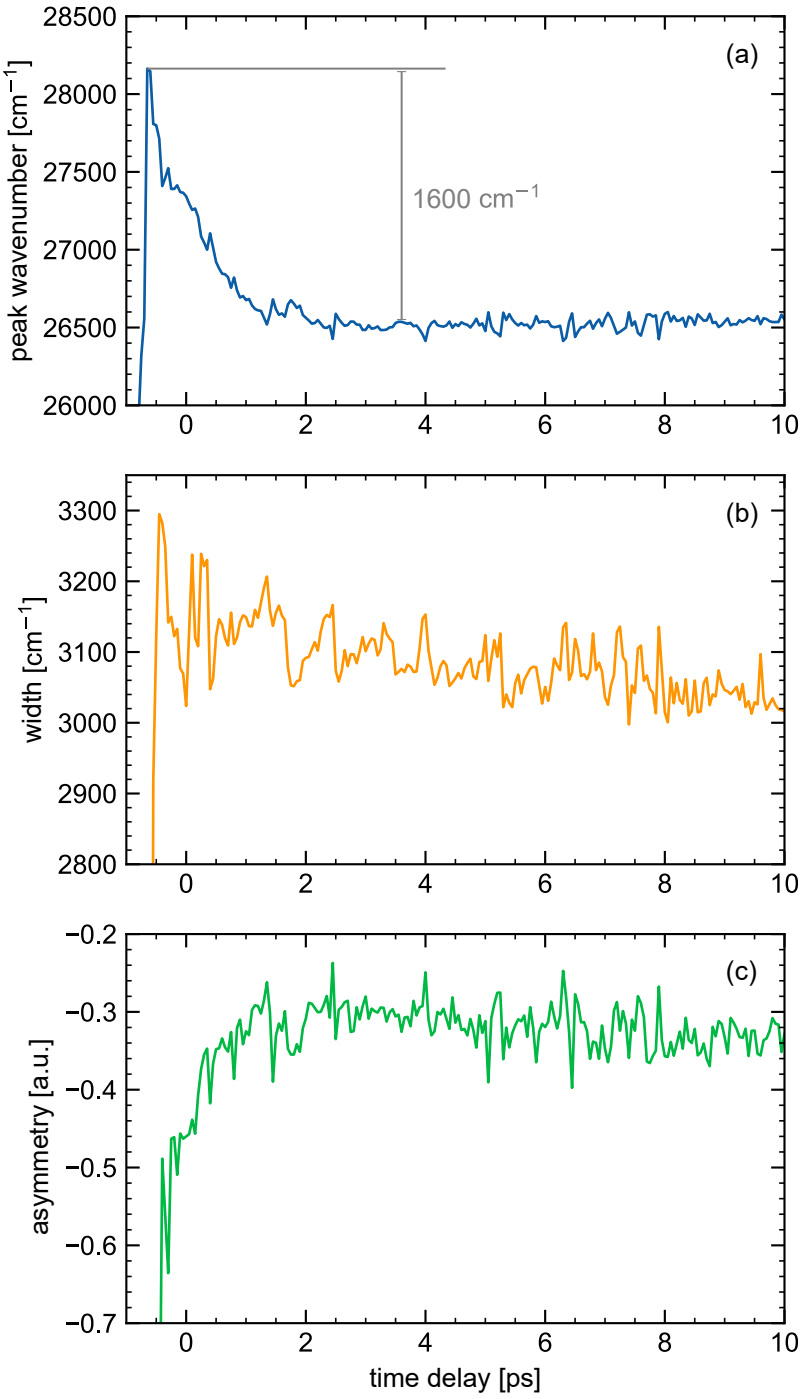

Figure 8.6: Evolution of lognormal parameters. Time-dependent parameters extracted from the spectral response of C153 in acetonitrile. A single lognormal function was used for fitting. It is consistent with a non-infinitesimal time resolution that the evolution of the lognormal parameters precedes time zero.

Conclusions

In this chapter, the newly installed FLUPS setup was characterized by measuring transient spectra of the known dye C153 in the subpicosecond regime. The spectra were not reconstructed using monochromatic measurements but recorded directly in a broadband fashion using tolerance phase-matching. Therefore, the photometric correction reported in the literature was carried out. It was not only shown that the correction procedure is necessary to obtain the true spectral response, but also that it is highly stable. Finally, the present setup was commissioned to reproduce the literature results concerning the spectral dynamics of C153. In summary, the functionality of the present setup has been proven such that it can be used to study other, less-studied systems.

9 CHAPTER

Characterization of the measurement modes

This chapter presents a complete characterization of the measurement modes called cases A and B. In the first section, C153 spectra and efficiency curves from the photometric correction are considered for both cases. Based on these, it is demonstrated that case A has a higher upconversion efficiency, whereas case B has better spectral coverage. The second section introduces a new data analysis strategy to retrieve in silico broadening of the spectral coverage. It is applied to case A and the results are compared with the conventional case B spectra. Finally, potential applications of this approach are discussed.

9.1 Comparison of cases A and B

In the preceding chapter, only the measurement mode with the name *case A* was applied. To understand and characterize both measurement modes, a series of analyzes was performed. Mutual agreement with the literature allows further conclusions on the operability of the FLUPS setup.

Transient upconversion spectra for cases A and B were acquired and photometric corrections were performed. The correction functions are calculated as described in chapter 7. Note that the transient spectra are not multiplied with the correction function as in chapter 8 because this would cause the loss of the peculiar features of cases A and B. Smoothened correction functions were used to calculate the upconversion efficiency $\eta = 1/\overline{c}$ as a function of wavelength. For this, a sample of C153 with $OD_{400\,nm} = 1.5$ was prepared and

steady-state t_∞ spectra were recorded. At this stage of work, ~100 µJ instead of ~200 µJ gate pulses and 0.5 s instead of 1 s exposure time were used. Therefore, the obtained count numbers are lower than those of chapter 8; other parameters were kept constant.

A comparison of the uncorrected t_∞ upconversion spectra is given in figure 9.1. The optimal phase-matching angle θ_{opt} was ~106° for case A and ~110° for case B.

On the top left, figure 7a presents the absolute signal captured in cases A (blue) and B (orange). Most strikingly, the count number at the peak is about three times higher in case A. The top right panel 7b displays the identical spectra but with normalized counts. It becomes apparent that the flanks of the peak exhibit more counts in case B, suggesting a broader spectral coverage. A quantitative analysis of the spectral coverage is given in figure 7c that shows a comparison of the normalized efficiency for both cases. While case A embraces a sharp maximum at ~390 nm and shows strong dispersion, case B demonstrates consistently high efficiency from 400 nm to 420 nm and comparatively low dispersion. However, both cases possess a weak performance "in the blue" that was already noted in chapter 8. *In toto*, the collected spectra and efficiency curves are qualitatively consistent with section 6.3, stating that case A is characterized by significantly increased efficiency at the cost of some spectral coverage compared to case B. Furthermore, quantitative coherence with the literature that is reporting an efficiency three to five times higher in case A can be concluded.

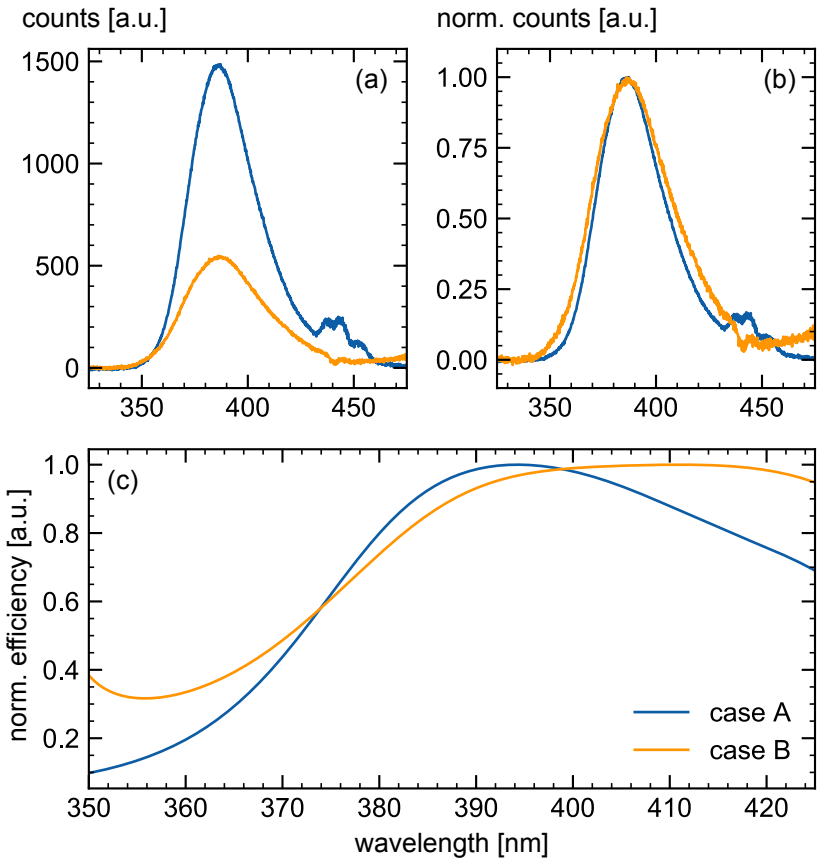

Figure 9.1: Experimental comparison of case A and case B. (a) Steady-state t_∞ spectra and (b) normalized t_∞ spectra as a function of wavelength; (c) Normalized upconversion efficiency η as a function of wavelength.

To fully characterize both measurement modes, it is indispensable to address their dependence on phase-matching angles. For this, the BBO was detuned by two degrees to the left and the right twice, respectively. The corresponding upconversion efficiencies $\eta(\theta)$ for the detuned angles were normalized and are depicted in figure 9.2. Note that the normalization is necessary for a reasonable comparison of the efficiency curves; their absolute magnitude decreases for larger detuning. Moreover, it can be noticed that the efficiency curves might diverge at particularly high or low wavelengths. This is due to an artifact in the calculation of the correction function and implies that the signal ends there.

In figures 9.2a and 9.2b (bottom panel; case B), five efficiency curves are presented, respectively. The blue curve conveys the optimal phase-matching instance that has already been considered in figure 9.1. Contrarily, the orange curves were recorded at lower and the green ones at higher phase-matching angles. It becomes evident that crystal rotation

towards smaller phase-matching angles increases the relative upconversion efficiency at smaller wavelengths, whereas a decline for larger wavelengths is observed simultaneously. A reverse effect can be witnessed for larger phase-matching angles. This behavior is expected because the phase-matching angle modifies the refractive index of the extraordinarily polarized gate. According to section 6.2, another fluorescence wavelength is now optimally upconverted and thus becomes the new central wavelength around which tolerance phase-matching is performed.

The comparison of the upper and lower panel illustrates that case A is significantly more responsive to detuned phase-matching angles, whereas case B remains approximately invariant to minor crystal rotation. This is because the dispersion in phase-mismatch is larger in case A (cf. section 6.3), and consequently it responds more sensitive to a variation in the central fluorescence wavelength. Therefore, the results are in line with the notion that case B has larger spectral coverage and shows lower dispersion.

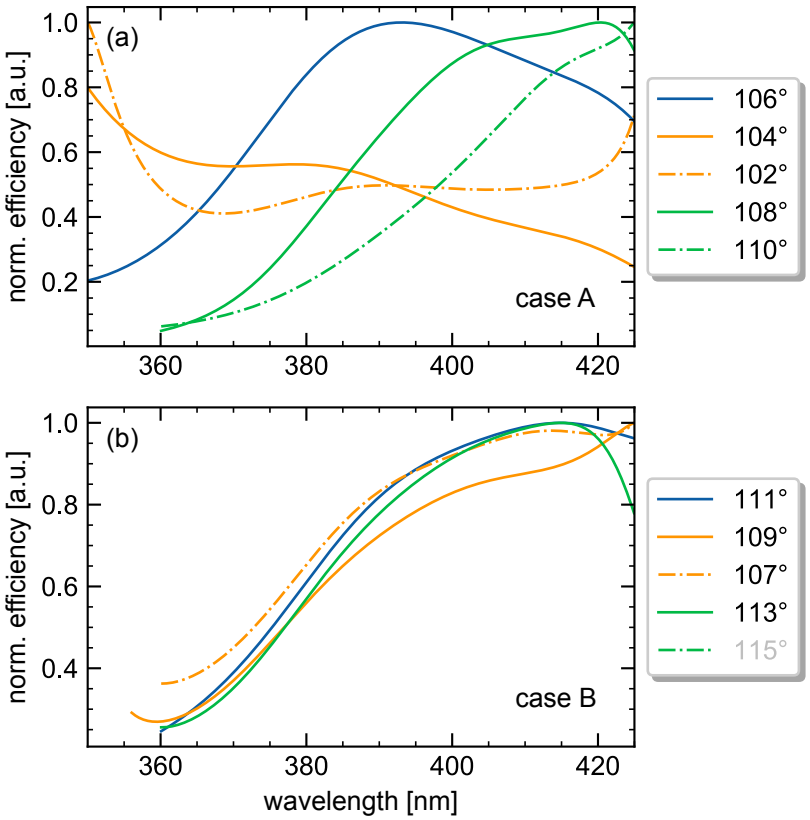

Figure 9.2: Efficiency curves $\eta(\theta)$ for cases A and B. Upconversion efficiency measured in (a) case A and (b) case B for different phase-matching angles.

Now, which of the measurement modes proves to be more valuable? This depends on the spectral particularities of the sample under investigation. For example, case A proves to be more useful for C153. Although the uncorrected spectra are narrower in case A, the lack of phase-matching bandwidth is compensated for by the photometric correction. However, for fluorescence of larger spectral widths, case A might fail to detect wavelengths at the peak edges. Such a situation is discussed in reference [97] using the molecule E-4-Dimethylamino-4'-nitrostilben (DANS). If the sample fluorescence is so broad that not all wavelengths can be effectively upconverted, a fix cannot be provided by the photometric correction. In this instance, case B could provide sufficient spectral coverage at the cost of signal intensity.

9.2 Synthetic aperture radar approach

Is it obligatory to use case B for broadening the spectral coverage? Indeed, it is also possible to reduce the crystal thickness, but the broadening effect is small and is accompanied by a non-negligible loss of efficiency. Another possibility based on data engineering is available for this purpose. It was orally proposed by N. P. Ernsting and involves taking a given series of transient scans as a measurement matrix $\underline{M} = (m_{\iota\upsilon})$ with the wavelength index ι and time index υ. The rows of $\underline{M}$ correspond to the transient spectra and the columns specify the different time traces.

As discussed, the upconversion efficiency is a function of the phase-matching angle. However, the true spectrum is not dependent on the instrumental bias, including the phase-matching angle. Therefore, the corresponding angle matrices $\underline{M}^{(\theta)}$ essentially contain similar information, just viewed from different phase-matching angles. This "viewing angle" is compensated for in the photometric correction, cf. chapter 7. Instead of looking at the angular matrices individually, the various angular aspects can also be combined into a single picture by using a "synthetic aperture radar" (SAR) like approach.

The SAR method is a data processing technique that is typically used in radar systems to resolve small objects on the ground. Its operating principle is outlined in figure 9.3a. Generally, the smaller the radar aperture, the longer is the corresponding radar antenna. This leads to an improved resolution. The length of the antennas is usually around five meters, but with the help of SAR, synthetic antenna lengths of up to 15 km can be achieved. For a synthesis, the antenna is moved past the ground objects, e.g. along the satellite's flight path, while transmitting pulses and receiving their echoes at regular intervals. In a

simplified picture, the echo signals are lined up along a trajectory so that they represent a single, large antenna. [98]

This concept can also be applied to FLUPS. Figure 9.3b shows how the upconverted PL spectra can be summed in the same manner for different phase-matching angles. For a fixed phase-matching angle, the correction function (here given by a parabola) specifies the phase-matching bandwidth. It might be insufficient to cover the entire spectral range. In such a scenario, the photometric can no longer compensate for a lack of phase-matching width. However, narrow spectral bandwidths originating from different phase-matching angles can be linked to receive a “synthetic phase-matching bandwidth”.

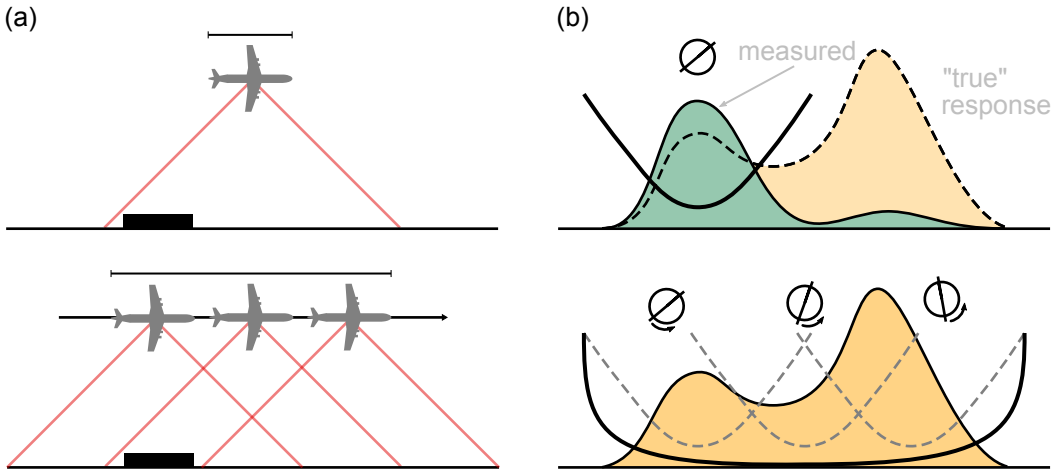

Figure 9.3: Concept behind the SAR method. (a) The synthetic aperture is artificially extended by lining up the antenna trail during radar translation; (b) If the phase-matching of a single angular matrix does not cover the whole spectral response, different ones can be combined. The result benefits from all phase-matching angles.

Referring to the angular matrices, the SAR approach is mathematically equivalent to the sum over all angular matrices with relative weights q_j:

$$\underline{M}^{\mathrm{SAR}} = \frac{1}{J} \sum_{j=1}^{J} q_j \underline{M}^{(\theta_j)}. \tag{9.1}$$

Application and discussion of SAR to FLUPS

To construct the angular matrices, the uncorrected steady-state t_∞ spectra from the previous section 9.1 were used. There were detected at five different angles, yielding five angular matrices. Then, the SAR matrix was constructed with equal coefficients, i.e. the mean of the angular matrices was calculated:

$$\underline{M}^{\mathrm{SAR}} = 0.2 \sum_{j=1}^{5} \underline{M}^{(\theta_j)}. \tag{9.2}$$

This choice of coefficients has proven to be particularly effective, both because of its simplicity and ideal noise reduction.[1] The construction of the SAR matrix for case A is exemplified in figure 9.4. The graphic depicts an averaged section of the rows, representing the respective t_∞ spectra, of each angle matrix (blue) and the resulting SAR matrix (orange). It becomes evident that the SAR spectrum has a lower peak intensity but benefits from the contributions of the detuned angular matrices at the fringes. Therefore, an increase in spectral coverage by SAR treatment is demonstrated.

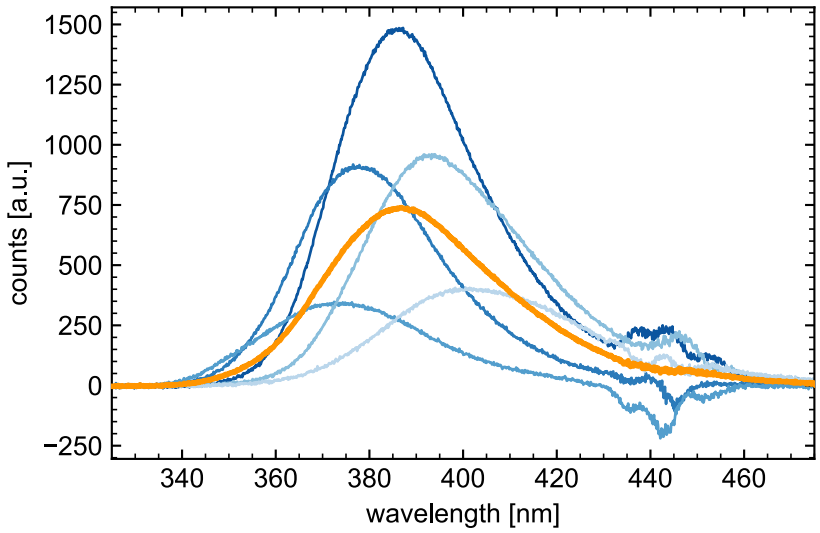

Figure 9.4: Construction of the SAR spectrum. The steady-state t_∞ SAR spectrum (orange, highlighted) is constructed by averaging the five respective t_∞ spectra obtained at different angles (blue).

[1] The averaging of ngular matrices corresponds to the integration over random noise, which obeys stochastic laws. The probabilities for the occurrence of a noise pattern per spectrum are equal, meaning that unequal coefficients will bias for a pattern.

Now the question arises of how large the broadening of the spectral coverage is and how severe the drop in intensity is after SAR treatment. For this purpose, a comparison of case A, case B, and the SAR treated case A, henceforth abbreviated *SAR A*, was performed. The results are summarized in figure 9.5. Note that the spectral coverage for the transient spectra is already maximized. This is because the use of a thinner crystal, which causes a wider phase-matching angle, does not broaden the spectral response in case B.

Figures 9.5a and 9.5b each display the normalized t_∞ spectrum (blue) as well as the upconversion efficiency (orange) for case A and SAR A. Both figures include the t_∞ spectrum measured in case B (gray) as well. Figure 9.5a illustrates the superior spectral coverage in case B that was already confirmed. A noticeable finding in figure 9.5b is that the spectra in case B and SAR A are almost identical, indicating that a significant broadening of the spectral coverage has been achieved using the SAR method. The comparatively good performance at the peak edges can also be perceived by the high normalized upconversion efficiency, which does not fall below a value of $1/3$. The absolute signal intensity is addressed in figure 9.5c. It provides a comparison of the absolute t_∞ spectra obtained employing SAR A and case B. Apparently, the signal peak of the SAR A spectrum contains $> 30\%$ more counts. Finally, figure 9.5d provides a direct comparison of the upconversion efficiencies in cases A, B, and SAR A. Interestingly, the SAR A efficiency curve approximates the one obtained in case B with very good agreement. This shows that SAR A successfully emulates the spectral coverage of case B. *In toto*, it can be deduced that SAR A delivers a better signal intensity than case B, while providing the same spectral coverage.

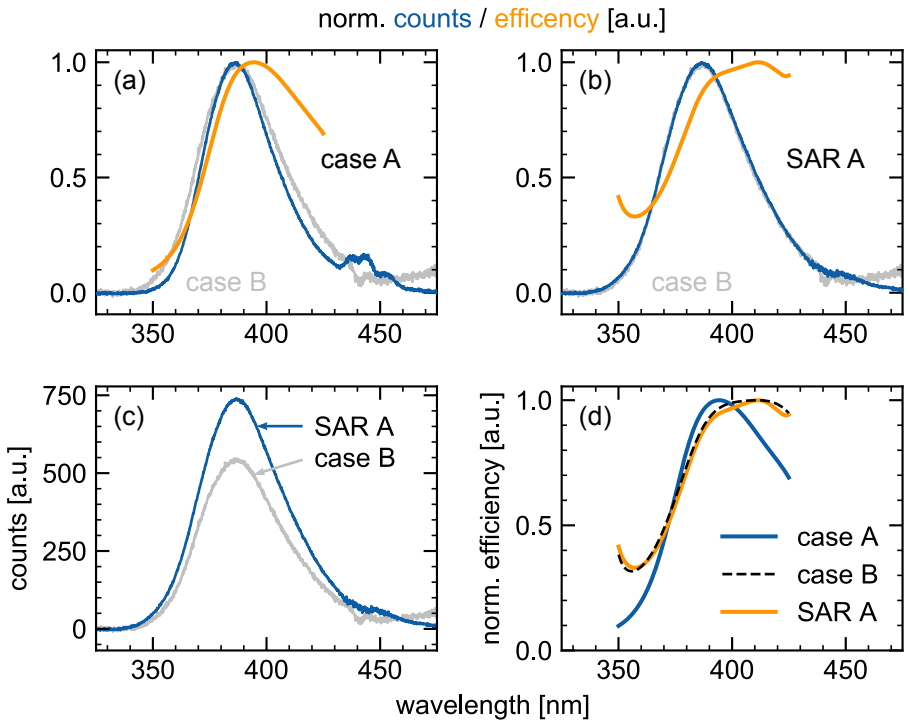

Figure 9.5: Conventional cases compared to SAR A. Normalized counts (blue) and upconversion efficiency (orange) in (a) case A and (b) SAR A, respectively. The normalized counts in case B are displayed in gray in both panels; (c) Absolute counts in SAR A and case B; (d) Normalized upconversion efficiency attained for cases A, B, and SAR A.

Recall that C153 displays identical normalized transient spectra for cases A and B after photometric correction, which emphasizes the high stability of this method described in chapter 8. Therefore, SAR treatment is not recommended for this fluorophore because suboptimal angular matrices $\theta \neq \theta_{\text{opt}}$ negatively affect the signal strength without spectral coverage benefits. Nonetheless, this section demonstrated the potential value of alternative data processing. Indeed, the spectral response of other samples might not be fully covered after photometric correction in case A but in case B. In such instances, the SAR approach is superior.

Conclusions

To summarize, the two measurement modes cases A and B have been compared in this chapter. It was experimentally confirmed that case A has a higher upconversion efficiency, whereas case B has better spectral coverage. The experimental results show excellent agreement with previous studies of Gerecke *et al.* Hence, the characterization of the FLUPS setup from the previous chapter has been expanded and can now be considered exhaustive. Furthermore, an alternative data analysis approach was transferred from the context of radar systems to time-resolved fluorescence for the first time. This approach was shown to improve the signal intensity while maintaining spectral coverage. Therefore, these findings have implications for future experiments dealing with broad emission responses.

10 CHAPTER

Towards upconversion of TMDC MLs

This chapter outlines the first important steps necessary to upconvert the emission from TMDC monolayers. First, the steps necessary to complete the transition from the C153 solution to WS_2 MLs are outlined. In particular, the new spectral properties pose a challenge that is addressed. Second, depletion spectra are used as strong evidence that the FLUPS setup is indeed able to upconvert the emission of 2D WS_2. Sources of the signal strength issue, preventing measurement of regular FLUPS spectra, are discussed.

10.1 From liquid to solid samples

OPTICALLY generated excitons in 2D TMDCs are an ideal system for exploring the novel properties of this material class. To date, research on their emission has mostly employed spectroscopy tools that can monitor their picosecond dynamics. With the fully characterized and operational FLUPS, first steps have been taken to investigate the bright decay of a TMDC sample on the femtosecond timescale. Because WS_2 has the highest quantum yield of the group IV TMDCs, it was chosen for subsequent investigations. For this, WS_2 MLs deposited on Si/SiO_2 were used. However, before the actual conversion experiment can be started, it is necessary to carry out some preparatory steps.

Preparatory steps

First, a dye is needed that covers a similar emission range as the WS_2 sample. A suitable candidate for this is DCM which was prepared as a solution in acetonitrile of optical density

$OD_{400\,nm} \approx 0.6$. A comparison of the normalized steady-state WS_2 and DCM emission spectra is given in figure 10.1a. The PL measurement of WS_2 was provided by B. T. Bonkano, who is a Ph.D. student in the electron dynamiX group. The spectral response of DCM was obtained by averaging FLUPS measurements in case A at steady-state time delays. Because the spectral response of WS_2 is narrow, the choice of case A is well justified. The emission peaks of both compounds lie near each other, while the spectral response of DCM is significantly higher.

Subsequently, the photometric correction was performed using the DCM solution. The conversion efficiency $\eta = 1/\overline{c}$ was calculated as described in chapter 7 and is plotted in figure 10.1b (green). Furthermore, the figure depicts the *in silico* upconverted steady-state WS_2 emission again. This demonstrates that the entire WS_2 emission range should be well covered by the correction function. Advantageously, the upconversion efficiency is at its maximum close to the emission peak. Therefore, the photometric correction is sufficiently prepared.

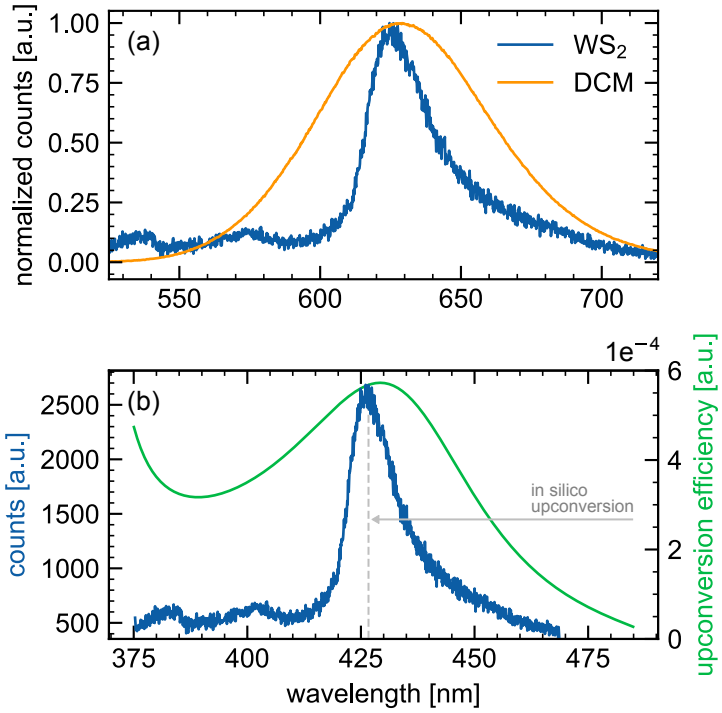

Figure 10.1: Comparison of WS_2 and DCM steady-state emission. (a) The peak of WS_2 at 627 nm almost overlaps with that of DCM at 629 nm; (b) The correction function covers the entire PL (upconverted representation) of the WS_2 sample.

Second, when working with MLs, two major drawbacks arise compared to liquid samples, which also have to be addressed. On the one hand, the damage threshold in solid samples decreases compared to those in liquid samples. This is because the atoms are in a rigid lattice, they cannot circulate as in molecules and are therefore exposed to constant and intense laser radiation. On the other hand, the number of atoms in MLs is very low, such that the absorbance (and thus the PL) is also low. This corresponds to a small molecular concentration that is roughly two orders of magnitude below the concentration where quenching effects will occur, cf. section 2.1.

To simulate these demanding conditions, the pump intensity was reduced to about 2% of the previous measurements, which is just below the damage threshold of the WS_2 MLs. Then a DCM mixture with optical density $OD_{400\,nm} \approx 0.07$ was prepared because at this concentration the solution has similar absorbance as the WS_2 sample. [99] The FLUPS signal was optimized again under the new circumstances. If all optics are aligned carefully, a weak but still recognizable signal can be received. Therefore it was shown that a signal can be detected even at very low pump intensities and the absorption level of 2D WS_2, at least for DCM.

Third, the altered emission properties pose a potential difficulty. Although TMDC MLs have a significantly higher quantum yield than the bulk [100], it is usually still < 1% due to defects. [101, 102] In contrast, laser dyes generally have a high quantum efficiency. For instance, the quantum yield of C153 amounts to $Q_{C153} = 54.4\,\%$. [103] However, not the quantum yield, but the detected photons per time interval are measured at the CCD camera. While a large quantum yield favors a high number of emitted photons, a short radiative lifetime is needed to produce a high “photon density" in the time domain. Fortunately, as discussed in chapter 3, a tiny radiative lifetime of < 1 ps are predicted in TMDC MLs. This is four orders of magnitude smaller than in standard dyes that typically have decay times of $\mathscr{T}_n \approx 10$ ns. Therefore, WS_2 samples are in theory well compatible with FLUPS, despite the small quantum yield. [20]

Finally, another challenge is the excitation wavelength. Usually, *Vavilov's rule* from chapter 2 is widely applicable for fluorescent samples. It states that the fluorescence quantum yield of a fluorophore is independent of the excitation wavelength. However, a publication around the research group of T. F. Heinz showed that this rule is not fulfilled by WS_2 MLs due to competing relaxation channels. [104] At the excitation wavelength of ~400 nm that is used in this setup, the quantum yield is < 10% of the yield obtained close to resonant excitation (~600 nm). Whether a perfectly resonant excitation at ~626 nm delivers even higher quantum yields remains open in reference [104]. This problem can be solved

through changing the excitation wavelength by modifying the optical setup. However, this reconstruction was outside the scope of this work. Given the study design, a significant loss of the achievable signal strength was inevitable. Additional information on estimating the signal strength can be found in appendix B11.

From liquid to solid samples

To move from liquid to solid samples, the DCM solution was replaced by WS_2 and the laser focus was adjusted by z-translation (the z-direction is the surface normal) of the sample holder. Note that the WS_2 sample is not homogeneous but single ML flakes are distributed on the substrate, see figure 10.2a. Through x and y-translation of the sample holder, the laser focus moves on the substrate. In contrast to DCM, the PL is not visible, so a camera was installed. At high exposure and integration time, weak emission of the MLs can be found when the sample holder is aligned correctly. The corresponding camera image is shown in figure 10.2b.

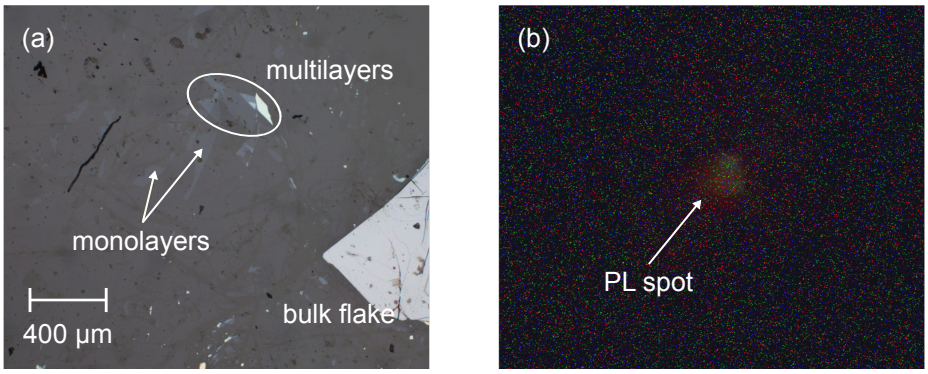

Figure 10.2: WS_2 sample and emission. (a) Optical microscopy image of the inhomogeneous WS_2 flakes on the silicon substrate. Monolayers are highlighted; (b) Camera image of the WS_2 sample surface upon radiation with the pump laser (with switched off ceiling lights). A faint red PL dot can be observed.

Although the camera provides evidence for PL emission, repeated attempts to detect an upconversion signal by FLUPS failed. This might be explained by the suboptimal excitation wavelength. However, because emission was observed by the camera, the absence of an upconverted signal raises another question: Is there no SFG at all due to the setup or is the signal strength below the instrument sensitivity?

10.2 Depletion spectroscopy

To test whether upconversion of the WS_2 emission occurs, depletion spectroscopy was introduced. [105] The essence of this spectroscopy is that PL and gate photons are consumed for the SFG during the upconversion process. Therefore, a decrease in the intensity of either pulse would indicate the presence of SFG. Because the gate pulse is very intense, it is a well-suited observable for depletion spectroscopy. However, it cannot be perceived as the setup is not capable of capturing infrared wavelengths. Fortunately, the third harmonic of the gate lies with ~450 nm within the accessible upconversion window. Consequently, it can be perceived in the background spectrum. Usually, the background is subtracted, but on this occasion, it happens to be the basis of depletion spectroscopy. Because THG is a third-order NLO process, it is proportional to I_g^3 and especially sensitive to changes in gate intensity. As a result, the third gate harmonic strongly depends on the upconversion efficiency and is the perfect observable to evaluate if upconversion takes place. Note that the gate intensity is also subject to fluctuations due to the finite stability of the laser, meaning that the fluctuations enter cubically in the background.

To perform depletion spectroscopy, the mechanical delay stage was manually shifted from t_0 to a slightly positive time delay < 1 ps. Then 100 spectra were acquired and summed at this position. Subsequently, the process was repeated for negative delay > −1 ps. The results are plotted in figure 10.3a. Interestingly, it can be seen that the intensity is lower during positive times. This indicates gate-depleting processes such as upconversion.

To examine the depletion process further, the difference spectrum ΔS was calculated according to

$$\Delta S = \frac{s(t > t_0) - s(t < t_0)}{s(t < t_0)} \tag{10.1}$$

It is shown in figure 10.3b (dark blue, highlighted). As expected for depletion, a negative signal is found in the region from 410 to 450 nm. To exclude the possibility that the signal is caused by gate fluctuations, the experiment was performed two more times (blue spectra D2 and D3, the corresponding background spectra are not displayed). Apparently, the depletion band roughly retains its shape and intensity for repeated measurements.

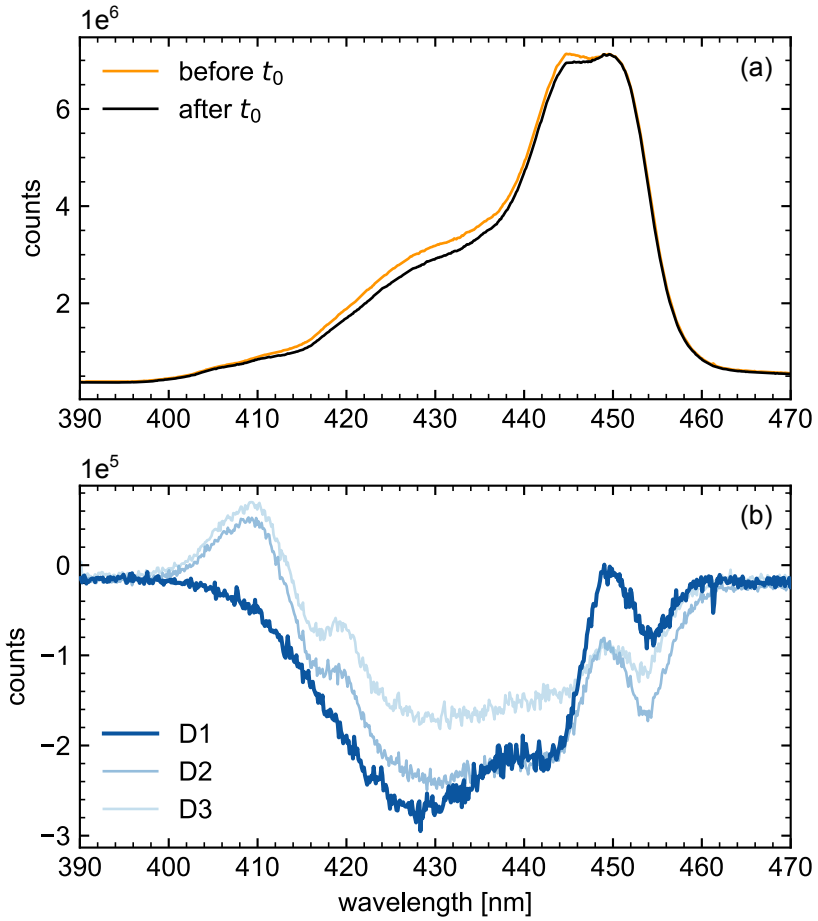

Figure 10.3: Background and difference spectra of WS_2. (a) Accumulated background spectra just before (black) and after (orange) excitation with the pump; (b) Difference spectra ΔS indicating gate depletion. Spectrum D1 was calculated from the background spectra of the upper panel, the spectra D2 and D3 represent replicate measurements.

Therefore, the continuous negative spectral signature observed in the difference spectra at the wavelengths regime of the third gate harmonics strongly indicates that an upconversion of the WS_2 emission is occurring. Nevertheless, extreme caution must be exercised in interpreting some of the spectral attributes found in figure 10.3b, because scatter of fluctuations might be wrongly assigned to excitonic processes. It can be assumed with a high probability that the peaks at ~410 nm are due to the scattering of the pump. Given the small sample size, an interpretation of the shape of the envelope and other peaks is refrained from at this point.

Conclusion

In summary, this chapter provides a significant first step towards upconverting the PL of TMDC MLs. The laser dye DCM was identified as optimal for the photometric correction. Moreover, the FLUPS design adapted to the requirements of the 2D WS_2 sample. Depletion spectroscopy provides strong evidence that PL upconversion of the TMDC monolayers was achieved for the first time, even if the signal intensity is not sufficient to obtain emission spectra yet. In fact, the results suggest that adjusting the excitation may be sufficient to increase the signal strength such that emission spectra are obtained.

11 CHAPTER

Summary and conclusion

THE present work had two major objectives:

(i) First, the commissioning of a FLUPS and its characterization concerning the functionality and the two different measurement modes A and B, respectively.

(ii) Second, the investigation of bright relaxation pathways in WS_2 on Si/SiO_2.

In the first part of this work, the FLUPS setup following N. P. Ernsting's design with femtosecond time resolution was implemented. However, FLUPS is a sensitive instrument with many potential sources of error. To prove its proper functionality, test measurements with the domestically studied dye C153 were performed and its solvation dynamics were monitored. For comparison with the literature, the experimental data were corrected for the apparatus bias by photometric correction. Based on the results, it can be deduced that the (re-)construction of the FLUPS was successful: A TDSS of ~1600 cm^{-1} was obtained for C153, which is in good agreement with previous studies.

Furthermore, novel research results of M. Gerecke *et al.* were considered and the reported measurement modes case A and case B were characterized. This work confirms that case A has approximately three times the signal strength but at the expense of some of the phase-matching bandwidth. Transient measurements of C153 at detuned phase-matching angles allowed to incorporate the SAR method. The posterior synthesis of those spectra enabled, for the first time, the *in silico* broadening of the phase-matching bandwidth. It also demonstrated the superiority of case A in combination with the SAR method over case B. However, the data gathering also suggested that the SAR method is not advantageous for regular applications due to the high stability of the photometric correction.

The second part of this work was devoted to the investigation of WS_2 MLs. For this purpose, a reference system was set up based on the dye DCM, whose radiation characteristics resemble those of the WS_2 sample to some extent. Fluorescence upconversion for the reference system was confirmed, but not directly detected for WS_2 MLs. However, depletion spectra suggest that SFG does take place, but the signal strength lies below the noise level. Finally, various reasons for the weak WS_2 emission were identified and promising solutions to the problem were proposed.

In conclusion, this thesis provides an initial step towards the study of TMDC MLs with FLUPS. On the one hand, the commissioning and characterization of the FLUPS setup was completed. The testing and standardization of the measurement instrument ensures that the experiments can be replicated and also carried out by other research groups. Moreover, a deeper understanding of FLUPS technical particularities that form the basis for further customization was obtained. On the other hand, close examination of TMDC MLs indicated that indeed further tailoring of the present setup is needed. Important tasks were identified that will lead to a successful upconversion of the emission. The next major step involves tuning the excitation wavelength to enhance the quantum yield of the WS_2 sample. Further efforts will be devoted to a pulse front tilt to improve the time resolution. In the short to medium term, it is anticipated that FLUPS measurements of WS_2 will be completed for the first time. Future research could follow up on FLUPS measurements of WS_2 MLs to determine similarities and differences in spectral and electronic properties between other TMDC MLs. Furthermore, new atomically thin architectures such as Van-der-Waals or organic-inorganic heterostructures based on TMDC MLs could also be investigated.

Bibliography

[1] K. S. Novoselov, A. K. Geim, S. V. Morozov, D. Jiang, Y. Zhang, S. V. Dubonos, I. V. Grigorieva, and A. A. Firsov. Electric Field Effect in Atomically Thin Carbon Films. *Science*, 306:666–669, 10 2004.

[2] R. Lv, J. A. Robinson, E. Schaak R, D. Sun, Y. Sun, T. E. Mallouk, and M. Terrones. Transition Metal Dichalcogenides and Beyond: Synthesis, Properties, and Applications of Single- and Few-Layer Nanosheets. *Accounts of Chemical Research*, 48:56–64, 1 2015.

[3] Q. H. Wang, K. Kalantar-Zadeh, A. Kis, J. N. Coleman, and M. S. Strano. Electronics and optoelectronics of two-dimensional transition metal dichalcogenides. *Nature Nanotechnology*, 7:699–712, 11 2012.

[4] B. Radisavljevic, A. Radenovic, J. Brivio, V. Giacometti, and A. Kis. Single-layer MoS2 transistors. *Nature Nanotechnology*, 6:147–150, 3 2011.

[5] T. Roy, M. Tosun, J. S. Kang, A. B. Sachid, S. B. Desai, M. Hettick, C. C. Hu, and A. Javey. Field-Effect Transistors Built from All Two-Dimensional Material Components. *ACS Nano*, 8:6259–6264, 6 2014.

[6] O. Lopez-Sanchez, D. Lembke, M. Kayci, A. Radenovic, and A. Kis. Ultrasensitive photodetectors based on monolayer MoS2. *Nature Nanotechnology*, 8:497–501, 7 2013.

[7] F. K. Perkins, A. L. Friedman, E. Cobas, P. M. Campbell, G. G. Jernigan, and B. T. Jonker. Chemical Vapor Sensing with Monolayer MoS2. *Nano Letters*, 13:668–673, 2 2013.

[8] F. Alharbi, J. D. Bass, A. Salhi, A. Alyamani, H.-C. Kim, and R. D. Miller. Abundant non-toxic materials for thin film solar cells: Alternative to conventional materials. *Renewable Energy*, 36:2753–2758, 10 2011.

[9] T. Chowdhury, E. C. Sadler, and T. J. Kempa. Progress and Prospects in Transition-Metal Dichalcogenide Research Beyond 2D. *Chemical Reviews*, 120:12563–12591, 11 2020.

[10] Q. Wang, S. Ge, X. Li, J. Qiu, Y. Ji, J. Feng, and D. Sun. Valley Carrier Dynamics in Monolayer Molybdenum Disulfide from Helicity-Resolved Ultrafast Pump–Probe Spectroscopy. *ACS Nano*, 7:11087–11093, 12 2013.

[11] C. Mai, A. Barrette, Y. Yu, Y. G. Semenov, K. W. Kim, L. Cao, and K. Gundogdu. Many-Body Effects in Valleytronics: Direct Measurement of Valley Lifetimes in Single-Layer MoS2. *Nano Letters*, 14:202–206, 1 2014.

[12] D. Sun, Y. Rao, G. A. Reider, G. Chen, Y. You, L. Brézin, A. R. Harutyunyan, and T. F. Heinz. Observation of Rapid Exciton–Exciton Annihilation in Monolayer Molybdenum Disulfide. *Nano Letters*, 14:5625–5629, 10 2014.

[13] C. Poellmann, P. Steinleitner, U. Leierseder, P. Nagler, G. Plechinger, M. Porer, R. Bratschitsch, C. Schüller, T. Korn, and R. Huber. Resonant internal quantum transitions and femtosecond radiative decay of excitons in monolayer WSe2. *Nature Materials*, 14:889–893, 9 2015.

[14] C. Robert, D. Lagarde, F. Cadiz, G. Wang, B. Lassagne, T. Amand, A. Balocchi, P. Renucci, S. Tongay, B. Urbaszek, and X. Marie. Exciton radiative lifetime in transition metal dichalcogenide monolayers. *Physical Review B*, 93:205423, 5 2016.

[15] S. Arzhantsev and M. Maroncelli. Design and characterization of a femtosecond fluorescence spectrometer based on optical kerr gating. *Appl. Spectrosc.*, 59:206–220, 2 2005.

[16] H. Chosrowjan, S. Taniguchi, and F. Tanaka. Ultrafast fluorescence upconversion technique and its applications to proteins. *The FEBS Journal*, 282:3003–3015, 8 2015.

[17] A. Krampf, S. Messerschmidt, and M. Imlau. Superposed picosecond luminescence kinetics in lithium niobate revealed by means of broadband fs-fluorescence upconversion spectroscopy. *Scientific Reports*, 10:11397, 12 2020.

[18] B. Bhattacharyya, A. Mukherjee, R. Mahadevu, and A. Pandey. Tuning radiative lifetimes in semiconductor quantum dots. *The Journal of Chemical Physics*, 154:074707, 2 2021.

[19] E. Socie, B. R. C. Vale, A. Burgos-Caminal, and J.-E. Moser. Direct Observation of Shallow Trap States in Thermal Equilibrium with Edge Excitons in Strongly Confined CsPbBr3 Perovskite Nanoplatelets. *Advanced Optical Materials*, 9:2001308, 1 2021.

[20] J. R. Lakowicz. *Principles of Fluorescence Spectroscopy*. Springer US, Boston, MA, 1999.

[21] J. Franck and E. G. Dymond. Elementary processes of photochemical reactions. *Transactions of the Faraday Society*, 21:536, 1926.

[22] Edward Condon. A Theory of Intensity Distribution in Band Systems. *Physical Review*, 28:1182–1201, 12 1926.

[23] M. Born and R. Oppenheimer. Zur Quantentheorie der Molekeln. *Annalen der Physik*, 389:457–484, 1927.

[24] S. Kumar Panigrahi and A. Kumar Mishra. Inner filter effect in fluorescence spectroscopy: As a problem and as a solution. *Journal of Photochemistry and Photobiology C: Photochemistry Reviews*, 41:100318, 12 2019.

[25] M. Sauer, J. Hofkens, and J. Enderlein. *Handbook of Fluorescence Spectroscopy and Imaging*. Wiley-VCH Verlag GmbH Co. KGaA, 1 2011.

[26] B. Bagchi and B. Jana. Solvation dynamics in dipolar liquids. *Chemical Society Reviews*, 39:1936, 2010.

[27] S. M. Sethna and N. M. Shah. The Chemistry of Coumarins. *Chemical Reviews*, 36(1):1–62, 1945.

[28] B. D. Wagner. The use of coumarins as environmentally-sensitive fluorescent probes of heterogeneous inclusion systems. *Molecules (Basel, Switzerland)*, 14(1):210–237, 2009.

[29] M. Maroncelli and G. R. Fleming. Picosecond solvation dynamics of coumarin 153: The importance of molecular aspects of solvation. *J. Chem. Phys.*, 86(11):6221–6239, 1987.

[30] M. Maroncelli and G. R. Fleming. Erratum: Picosecond solvation dynamics of coumarin 153: The importance of molecular aspects of solvation [J. Chem. Phys. 86 , 6221 (1987)]. *J. Chem. Phys.*, 92(5):3251, 1990.

[31] I. Eom and T. Joo. Polar solvation dynamics of coumarin 153 by ultrafast time-resolved fluorescence. *Journal of Chemical Physics*, 131(24):244507, 2009.

[32] X-X Zhang, C. Würth, L. Zhao, U. Resch-Genger, N. P. Ernsting, and M. Sajadi. Femtosecond broadband fluorescence upconversion spectroscopy: improved setup and photometric correction. *Review of Scientific Instruments*, 82(6):063108, 2011.

[33] M. Maroncelli, X.-X. Zhang, M. Liang, D. Roy, and N. P. Ernsting. Measurements of the complete solvation response of coumarin 153 in ionic liquids and the accuracy of simple dielectric continuum predictions. *Faraday Discussions*, 154:409–24; discussion 439–64, 465–71, 2012.

[34] X.-X. Zhang, M. Liang, N. P. Ernsting, and M. Maroncelli. Complete solvation response of coumarin 153 in ionic liquids. *The Journal of Physical Chemistry B*, 117(16):4291–4304, 2013.

[35] S. S. Chou, N. Sai, P. Lu, E. N. Coker, S. Liu, K. Artyushkova, Ting S. Luk, B. Kaehr, and C. J. Brinker. Understanding catalysis in a multiphasic two-dimensional transition metal dichalcogenide. *Nature Communications*, 6:8311, 11 2015.

[36] K. S. Novoselov, D. Jiang, F. Schedin, T. J. Booth, V. V. Khotkevich, S. V. Morozov, and A. K. Geim. Two-dimensional atomic crystals. *Proceedings of the National Academy of Sciences*, 102:10451–10453, 7 2005.

[37] J. N. Coleman, M. Lotya, A. O'Neill, S. D. Bergin, P. J. King, U. Khan, K. Young, A. Gaucher, S. De, R. J. Smith, I. V. Shvets, S. K. Arora, G. Stanton, H.-Y. Kim, K. Lee, G. T. Kim, G. S. Duesberg, T. Hallam, J. J. Boland, J. J. Wang, J. F. Donegan, J. C. Grunlan, G. Moriarty, A. Shmeliov, R. J. Nicholls, J. M. Perkins, E. M. Grieveson, K. Theuwissen, D. W. McComb, P. D. Nellist, and V. Nicolosi. Two-Dimensional Nanosheets Produced by Liquid Exfoliation of Layered Materials. *Science*, 331:568–571, 2 2011.

[38] Y. Zhan, Z. Liu, S. Najmaei, P. M. Ajayan, and J. Lou. Large-Area Vapor-Phase Growth and Characterization of MoS2 Atomic Layers on a SiO2 Substrate. *Small*, 8:966–971, 4 2012.

[39] K. F. Mak, C. Lee, J. Hone, J. Shan, and T. F. Heinz. Atomically Thin MoS2: A New Direct-Gap Semiconductor. *Physical Review Letters*, 105:136805, 9 2010.

[40] H. Terrones, F. Lopez-Urías, and M. Terrones. Novel hetero-layered materials with tunable direct band gaps by sandwiching different metal disulfides and diselenides. *Scientific Reports*, 3:1549, 12 2013.

[41] K. Kośmider, J. W. González, and J. Fernández-Rossier. Large spin splitting in the conduction band of transition metal dichalcogenide monolayers. *Physical Review B*, 88:245436, 12 2013.

[42] A. Kormányos, G. Burkard, M. Gmitra, J. Fabian, V. Zólyomi, N. D Drummond, and V. Fal'ko. k*p theory for two-dimensional transition metal dichalcogenide semiconductors. *2D Materials*, 2:022001, 4 2015.

[43] A. Kormányos, G. Burkard, M. Gmitra, J. Fabian, V. Zólyomi, N. D. Drummond, and V. Fal'ko. Corrigendum: k*p theory for two-dimensional transition metal dichalcogenide semiconductors. *2D Materials*, 2:049501, 11 2015.

[44] G. Wang, A. Chernikov, M. M. Glazov, T. F. Heinz, X. Marie, T. Amand, and B. Urbaszek. Colloquium : Excitons in atomically thin transition metal dichalcogenides. *Reviews of Modern Physics*, 90(2), 2018.

[45] T. Mueller and E. Malic. Exciton physics and device application of two-dimensional transition metal dichalcogenide semiconductors. *npj 2D Materials and Applications*, 2:29, 12 2018.

[46] A. Y. Joe. *Interlayer Excitons in Atomically Thin van der Waals Semiconductor Heterostructures*. PhD thesis, 2021.

[47] B. Zhu, X. Chen, and X. Cui. Exciton Binding Energy of Monolayer WS2. *Scientific Reports*, 5:9218, 8 2015.

[48] A. R. Klots, A. K. M. Newaz, B. Wang, D. Prasai, H. Krzyzanowska, J. Lin, D. Caudel, N. J. Ghimire, J. Yan, B. L. Ivanov, K. A. Velizhanin, A. Burger, D. G. Mandrus, N. H. Tolk, S. T. Pantelides, and K. I. Bolotin. Probing excitonic states in suspended two-dimensional semiconductors by photocurrent spectroscopy. *Scientific Reports*, 4:6608, 5 2015.

[49] A. Chernikov, T. C. Berkelbach, H. M. Hill, A. Rigosi, Y. Li, O. B. Aslan, D. R. Reichman, M. S. Hybertsen, and T. F. Heinz. Exciton Binding Energy and Nonhydrogenic Rydberg Series in Monolayer WS2. *Physical Review Letters*, 113:076802, 8 2014.

[50] K. He, N. Kumar, L. Zhao, Z. Wang, K. F. Mak, H. Zhao, and J. Shan. Tightly Bound Excitons in Monolayer WSe2. *Physical Review Letters*, 113:026803, 7 2014.

[51] H. Wang, C. Zhang, W. Chan, C. Manolatou, S. Tiwari, and F. Rana. Radiative lifetimes of excitons and trions in monolayers of the metal dichalcogenide MoS2. *Physical Review B*, 93:045407, 1 2016.

[52] M. Palummo, M. Bernardi, and J. C. Grossman. Exciton Radiative Lifetimes in Two-Dimensional Transition Metal Dichalcogenides. *Nano Letters*, 15:2794–2800, 5 2015.

[53] R. Trebino. *Frequency-Resolved Optical Gating: The Measurement of Ultrashort Laser Pulses*. Springer US, Boston, MA, 2000.

[54] V. I. Minkin. Glossary of terms used in theoretical organic chemistry. *Pure and Applied Chemistry*, 71(10):1919–1981, 1999.

[55] J. A. Armstrong, N. Bloembergen, J. Ducuing, and P. S. Pershan. Interactions between Light Waves in a Nonlinear Dielectric. *Physical Review*, 127(6):1918–1939, 1962.

[56] N. Bloembergen and P. S. Pershan. Light Waves at the Boundary of Nonlinear Media. *Physical Review*, 128(2):606–622, 1962.

[57] J. A. Giordmaine. Mixing of Light Beams in Crystals. *Physical Review Letters*, 8(1):19–20, 1962.

[58] R. L. Byer. Nonlinear Optical Phenomena and Materials. *Annual Review of Materials Science*, 4(1):147–190, 1974.

[59] H. Mahr and M. D. Hirsch. An optical up-conversion light gate with picosecond resolution. *Opt. Commun.*, 13(2):96–99, 1975.

[60] M. Sajadi, M. Quick, and N. P. Ernsting. Femtosecond broadband fluorescence spectroscopy by down- and up-conversion in b-barium borate crystals. *Applied Physics Letters*, 103(17):173514, 2013.

[61] H. Chosrowjan, editor. *Fluorescence up-conversion Methods and Applications (in: Encyclopedia of Spectroscopy and Spectrometry)*. Elsevier, 2017.

[62] N. P. Ernsting. FLUPS Manual (internal document).

[63] N. P. Ernsting, J. Breffke, D. Y. Vorobyev, D. A. Duncan, and I. Pfeffer. Sub-picosecond fluorescence evolution of amino-cyano-stilbenes in methanol: polar solvation obeys continuum theory without evidence of twisting. *Phys. Chem. Chem. Phys.*, 10(15):2043–2049, 2008.

[64] M. Sajadi, A. L. Dobryakov, E. Garbin, N. P. Ernsting, and S. A. Kovalenko. Time-resolved fluorescence spectra of cis-stilbene in hexane and acetonitrile. *Chemical Physics Letters*, 489(1-3):44–47, 2010.

[65] S. B. Desai, S. R. Madhvapathy, M. Amani, D. Kiriya, M. Hettick, M. Tosun, Y. Zhou, M. Dubey, J. W. Ager, D. Chrzan, and A. Javey. Gold-Mediated Exfoliation of Ultralarge Optoelectronically-Perfect Monolayers. *Advanced Materials*, 28:4053–4058, 6 2016.

[66] F. Liu, M. E. Ziffer, K. R. Hansen, J. Wang, and X. Zhu. Direct Determination of Band-Gap Renormalization in the Photoexcited Monolayer MoS2. *Physical Review Letters*, 122:246803, 6 2019.

[67] M. A. Kahlow, W. Jarzeba, T. P. DuBruil, and P. F. Barbara. Ultrafast emission spectroscopy in the ultraviolet by time–gated upconversion. *Rev. Sci. Instrum.*, 59(7):1098–1109, 1988.

[68] J. Shah. Ultrafast luminescence spectroscopy using sum frequency generation. *IEEE Journal of Quantum Electronics*, 24(2):276–288, 1988.

[69] J. Xu and J. R. Knutson, editor. *Ultrafast Fluorescence Spectroscopy via Upconversion (in: Fluorescence Spectroscopy)*, volume 450 of *Methods in Enzymology*. Elsevier, 2008.

[70] A. Yariv and P. Yeh. *Photonics: Optical electronics in modern communications*. The Oxford series in electrical and computer engineering. Oxford University Press, New York, NY, 6. edition edition, 2007.

[71] D. N. Nikogosyan. *Nonlinear Optical Crystals: A Complete Survey*. Springer Science+Business Media Inc, New York, NY, 2005.

[72] L. Zhu, X. Zhang, M. Xu, B. Liu, S. Ji, L. Zhang, H. Zhou, F. Liu, Z. Wang, and X. Sun. Refractive indices in the whole transmission range of partially deuterated KDP crystals. *AIP Advances*, 3(11):112114, 2013.

[73] L. Zhao, J. Luis Pérez Lustres, V. Farztdinov, and N. P. Ernsting. Femtosecond fluorescence spectroscopy by upconversion with tilted gate pulses. *Physical Chemistry Chemical Physics*, 7(8):1716–1725, 2005.

[74] W. von Sellmeier. Zur Erklärung der abnormen Farbenfolge im Spectrum einiger Substanzen. *Annalen der Physik und Chemie*, 219(6):272–282, 1871.

[75] K. Kato. Second-harmonic generation to 2048 Å in B-Ba2O4. *IEEE Journal of Quantum Electronics*, 22(7):1013–1014, 1986.

[76] R. Jimenez, G. R. Fleming, P. V. Kumar, and M. Maroncelli. Femtosecond solvation dynamics of water. *Nature*, 369(6480):471–473, 1994.

[77] H. S. Cho, H. Rhee, J. K. Song, C.-K. Min, M. Takase, N. Aratani, S. Cho, A. Osuka, T. Joo, and D. Kim. Excitation energy transport processes of porphyrin monomer, dimer, cyclic trimer, and hexamer probed by ultrafast fluorescence anisotropy decay. *Journal of the American Chemical Society*, 125(19):5849–5860, 2003.

[78] Y.-T. Kao, C. Saxena, T.-F. He, L. Guo, L. Wang, A. Sancar, and D. Zhong. Ultrafast dynamics of flavins in five redox states. *J. Am. Chem. Soc.*, 130(39):13132–13139, 2008.

[79] L. Zhang, Y. Yang, Y.-T. Kao, L. Wang, and D. Zhong. Protein hydration dynamics and molecular mechanism of coupled water-protein fluctuations. *Journal of the American Chemical Society*, 131(30):10677–10691, 2009.

[80] M. L. Horng, J. A. Gardecki, A. Papazyan, and M. Maroncelli. Subpicosecond Measurements of Polar Solvation Dynamics: Coumarin 153 Revisited. *The Journal of Physical Chemistry*, 99(48):17311–17337, 1995.

[81] J. A. Gardecki and M. Maroncelli. Comparison of the Single-Wavelength and Spectral-Reconstruction Methods for Determining the Solvation-Response Function. *The Journal of Physical Chemistry A*, 103(9):1187–1197, 1999.

[82] K. Ding, S. J. Courtney, A. J. Strandjord, S. Flom, D. Friedrich, and P. F. Barbara. Excited-state intramolecular proton transfer and vibrational relaxation in 2-(2-hydroxyphenyl)benzothiazole. *The Journal of Physical Chemistry*, 87(7):1184–1188, 1983.

[83] T. Gustavsson, G. Baldacchino, J.-C. Mialocq, and S. Pommeret. A femtosecond fluorescence up-conversion study of the dynamic Stokes shift of the DCM dye molecule in polar and non-polar solvents. *Chemical Physics Letters*, 236(6):587–594, 1995.

[84] T. Gustavsson, L. Cassara, V. Gulbinas, G. Gurzadyan, J.-C. Mialocq, S. Pommeret, M. Sorgius, and P. van der Meulen. Femtosecond Spectroscopic Study of Relaxation Processes of Three Amino-Substituted Coumarin Dyes in Methanol and Dimethyl Sulfoxide. *The Journal of Physical Chemistry A*, 102(23):4229–4245, 1998.

[85] S. Haacke, R. A. Taylor, I. Bar-Joseph, M. J. S. P. Brasil, M. Hartig, and B. Deveaud. Improving the signal-to-noise ratio of femtosecond luminescence upconversion by multichannel detection. *Journal of the Optical Society of America B*, 15(4):1410, 1998.

[86] A. Cannizzo, O. Bräm, G. Zgrablic, A. Tortschanoff, A. Ajdarzadeh Oskouei, F. van Mourik, and M. Chergui. Femtosecond fluorescence upconversion setup with broadband detection in the ultraviolet. *Optics Letters*, 32(24):3555–3557, 2007.

[87] R. Schanz, S. A. Kovalenko, V. Kharlanov, and N. P. Ernsting. Broad-band fluorescence upconversion for femtosecond spectroscopy. *Applied Physics Letters*, 79(5):566–568, 2001.

[88] M. Gerecke, G. Bierhance, M. Gutmann, N. P. Ernsting, and A. Rosspeintner. Femtosecond broadband fluorescence upconversion spectroscopy: Spectral coverage versus efficiency. *Review of Scientific Instruments*, 87(5):053115, 2016.

[89] J. A. Gardecki and M. Maroncelli. Set of Secondary Emission Standards for Calibration of the Spectral Responsivity in Emission Spectroscopy. *Appl. Spectrosc. (Applied Spectroscopy)*, 52(9):1179–1189, 1998.

[90] J. Mooney and P. Kambhampati. Get the Basics Right: Jacobian Conversion of Wavelength and Energy Scales for Quantitative Analysis of Emission Spectra. *The Journal of Physical Chemistry Letters*, 4(19):3316–3318, 2013.

[91] J. Mooney and P. Kambhampati. Correction to "Get the Basics Right: Jacobian Conversion of Wavelength and Energy Scales for Quantitative Analysis of Emission Spectra". *The Journal of Physical Chemistry Letters*, 5(20):3497, 2014.

[92] D. B. Siano and D. E. Metzler. Band Shapes of the Electronic Spectra of Complex Molecules. *The Journal of Chemical Physics*, 51:1856–1861, 9 1969.

[93] E. A. Burstein and V. I. Emelyanenko. Log-Normal Description of Fluorescence Spectra of Organic Fluorophores. *Photochemistry and Photobiology*, 64:316–320, 8 1996.

[94] T. Elsaesser and W. Kaiser. Vibrational and Vibronic Relaxation of Large Polyatomic Molecules in Liquids. *Annual Review of Physical Chemistry*, 42:83–107, 10 1991.

[95] H. R. Schanz. Femtosecond broadbandfluorescence upconversion, 2002.

[96] S. Arzhantsev and M. Maroncelli. Design and characterization of a femtosecond fluorescence spectrometer based on optical Kerr gating. *Applied Spectroscopy*, 59(2):206–220, 2005.

[97] M. Gerecke. *Femtosekunden-zeitaufgelöste Fluoreszenzspektroskopie von solvatochromen Sonden: Eine Suche nach lokaler Wasserdynamik*. PhD thesis, 2017.

[98] Deutsches Zentrum für Luft- und Raumfahrt. Synthetic aperture radar (sar).

[99] B. T. Bonkano. Oral communication.

[100] H. R. Gutiérrez, N. Perea-López, A. L. Elías, A. Berkdemir, B. Wang, R. Lv, F. López-Urías, V. H. Crespi, H. Terrones, and M. Terrones. Extraordinary room-temperature photoluminescence in triangular WS2 monolayers. *Nano Letters*, 13(8):3447–3454, 2013.

[101] L. Yuan and L. Huang. Exciton dynamics and annihilation in WS2 2D semiconductors. *Nanoscale*, 7(16):7402–7408, 2015.

[102] S. Roy, A. S. Sharbirin, Y. Lee, W. B. Kim, T. S. Kim, K. Cho, K. Kang, H. S. Jung, and J. Kim. Measurement of Quantum Yields of Monolayer TMDs Using Dye-Dispersed PMMA Thin Films. *Nanomaterials*, 10(6), 2020.

[103] K. Rurack and M. Spieles. Fluorescence quantum yields of a series of red and near-infrared dyes emitting at 600-1000 nm. *Analytical Chemistry*, 83(4):1232–1242, 2011.

[104] H. M. Hill, A. F. Rigosi, C. Roquelet, A. Chernikov, T. C. Berkelbach, D. R. Reichman, M. S. Hybertsen, L. E. Brus, and T. F. Heinz. Observation of Excitonic Rydberg States in Monolayer MoS2 and WS2 by Photoluminescence Excitation Spectroscopy. *Nano Letters*, 15(5):2992–2997, 2015.

[105] M. J. Côté, J. F. Kauffman, P. G. Smith, and J. D. McDonald. Picosecond fluorescence depletion spectroscopy. I. Theory and apparatus. *Journal of Chemical Physics*, 90(6):2865–2873, 1989.

Appendix A: Pulse Tilt

THE time resolution in the experiments of this work was ~400 fs. However, in the literature, time resolutions with $\Delta t < 100$ fs have been reported. To accomplish this, the gate pulse needs to be tilted with a certain angle Φ by a third prism Pr3 as shown in figure 11.1a: While the ray at the top passes through prism material, the ray at the bottom crosses the apex. Consequently, the propagation time from line X to Y results in the difference [73]

$$\Delta\tau = \tau_{\text{top}} - \tau_{\text{bottom}} = \frac{2L_{\text{top}}}{v_{\text{g}}(\omega)} - \frac{2L_{\text{bottom}}}{\text{c}}, \tag{11.1}$$

where $v_{\text{g}}(\omega) = \partial\omega/\partial k$ is the group velocity. It is the velocity with which the envelope of the gate propagates in the prism Pr3, therefore $v_{\text{g}}(\omega) < \text{c}$. The tilt angle Φ can be geometrically calculated:

$$\Phi = \arctan\left(\frac{\text{c}\Delta\tau}{w_0}\right). \tag{11.2}$$

Here, w_0 is the distance between the two boundary rays.

Figure 11.1b shows how the fluorescence and gate beams interact with and without a tilted gate pulse. It can be seen that the time resolution is limited due to the interaction angle α'. The corresponding front shearing results into a loss of resolution, which is avoided by a tilted gate pulse. To completely avoid a front shearing, the tilt angle must be equal to the interaction angle α'. However, the desired angle can usually not be attained using a prism alone. That is why lens L can be employed to amplify the tilt and map Φ onto α'. Despite its strong advantages, gate tilting has not been applied in this work because it caused problems with the focus. Nevertheless, gate tilting represents a promising improvement of the present setup in the future.

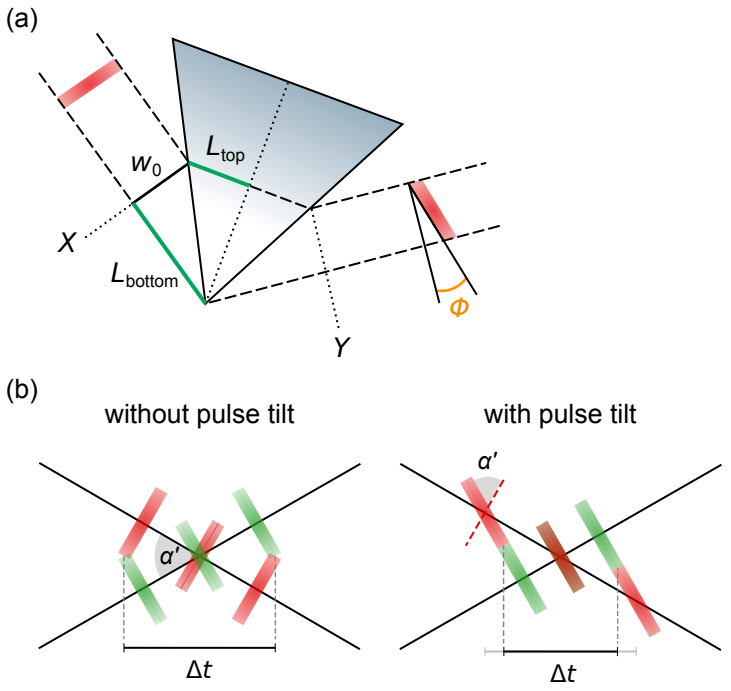

Figure 11.1: Pulse tilt. (a) The gate pulse is tilted using a prism; (b) Pulse tilting avoids front shearing between fluorescence and gat pulse whicht resuls in improved time resolution.

Appendix B: TCSPC measurements

TIME-CORRELATED SINGLE-PHOTON COUNTING (TCSPC) is a common technique for measuring emission decays with picosecond time resolution. In this method, the sample is initially excited by a laser pulse. The subsequent emission is detected with a high-gain photomultiplier tube and the time to the first detected photon event is recorded. By counting many single-photon events, a histogram of the photon distribution over time (and spatial coordinates) is constructed. It reflects the exponential decay of the emission intensity.

Although the time resolution of TCSPC is, with a few picoseconds, significantly worse compared to FLUPS, it is much easier to perform and has a very high sensitivity. Therefore, it is capable of detecting the weak emission of WS_2.

To compare the signal strength of the DCM and WS_2 emission, TCSPC measurements were performed. The DCM sample in acetonitrile with $OD_{400\,nm} = 0.07$ from section 10.1 was used because its absorbance is comparable to WS_2 on Si/SiO_2 at 400 nm excitation. Then, photon histograms for both samples were recorded and are shown in figure 11.2. Evidently, DCM exhibits significantly higher count numbers over the entire time and decays much more slowly compared to the TMDC.

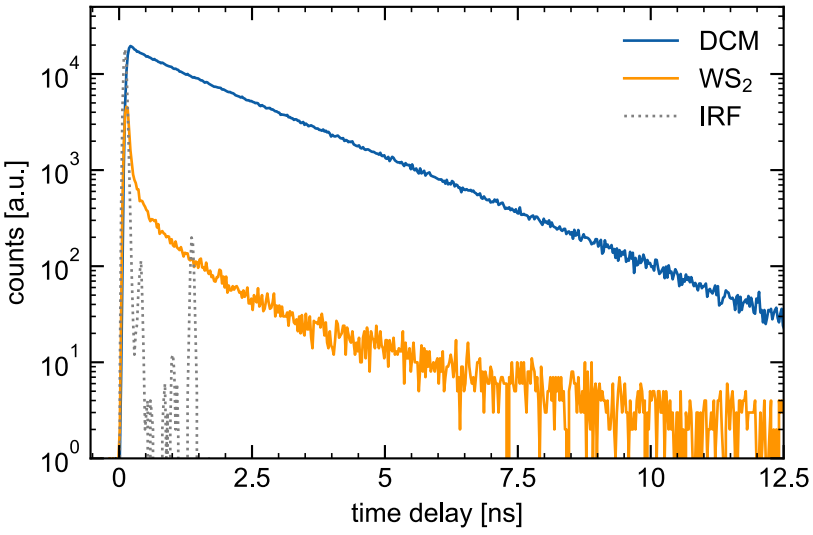

Figure 11.2: TCSPC spectra of DCM and WS_2. The histograms were recorded after excitation with 400 nm and are displayed on a logarithmic scale. Apparently, both the signal intensity and decay time are significantly smaller for WS_2 than those of DCM.

The TCSPC data from figure 11.2 were used to compute a rough estimate of the expected signal strength of WS_2 in FLUPS. Of course, the signal strength of TCSPC cannot be directly transferred to FLUPS, if only because the time resolution is different. Therefore, the following consideration can only be of qualitative character. However, the prove instructive nonetheless.

According to the logarithmic intensity scale, the DCM signal is ~100 times stronger than that of WS_2. This can be explained by the significantly lower quantum yield of WS_2 MLs. This effect is further enhanced by the suboptimal excitation wavelength at 400 nm, cf. section 10.1. Futhermore, FLUPS measurements of DCM are available. These were also performed at 400 nm excitation and low pump intensities (at the WS_2 damage threshold level). At best, the upconverted spectra provided a few hundred counts at 1 s exposure time, while the noise was ~20 counts. If the PL intensity of the WS_2 MLs is assumed to behave analogously as in TCSPC, then it would lie about a factor of ten below the noise floor in FLUPS. Therefore, it seems unambiguous that the PL of WS_2 cannot be detected in FLUPS when excited at 400 nm, which is supported by the findings from section 10.2.

Index

Nomenclature

$C(\tau)$	Cross-correlation function between pump and gate.
E	Electromagnetic pulse (field).
E_b	Exciton binding energy.
E_exc	Exciton emission energy.
E_g	Bandgap energy.
I	(Pulse) intensity.
L	Crystal thickness.
P	Electric polarization (field).
Q	Quantum yield.
V_c	Coulomb potential.
ΔS	Difference spectrum.
$\Delta\tau$	Difference in propagation time.
Δk	Phase-mismatch.
Δt	Time resolution.
α'	External interaction angle between fluorescence and gate pulse.
$\chi^{(j)}$	Electric susceptibility of j-th order.
δ	Angle of incidence between the considered pulse and the surface normal.
γ	Asymmetry parameter of a lognormal function.
$\hat{H}$	Hamiltonian (operator corresponding to the total energy of a system).

$\hbar$ Reduced Planck constant.

$[F^*(t)]$ Population of excited fluorophores as a function of time.

$\mathscr{T}$ Observed fluorescence lifetime.

$\mathscr{T}_{\mathrm{n}}$ Natural radiative lifetime.

IRF Instrument response function.

OD Optical density.

a_0 Bohr radius of the hydrogen atom.

c Speed of light in vacuum.

h Planck constant.

μ_0 Magnetic permeability of free space.

ν Frequency of light.

σ Total number of detected signal counts.

τ Time delay between pump and probe pulses.

θ Phase-matching angle.

θ_{opt} Optimal phase-matching angle.

$\tilde{\nu}_0$ Peak wavenumber parameter of a lognormal function.

$\underline{M}$ Measurement matrix.

μ Two-body reduced mass.

Δ Bandwidth wavenumber parameter of a lognormal function.

Γ_{nr} Non-radiative decay rate.

Γ_{r} Radiative decay rate.

Φ Tilt angle of the gate.

ε Absolute permittivity.

ε_0 Vacuum permittivity.

ε_{r} Dielectric constant (permittivity) of the crystal lattice.

a	Amplitude parameter of a lognormal function.
$a_{\mathrm{B}}^{\mathrm{2D}}$	Bohr radius of 2D excitons.
a_{l}	Lattice constant.
c	Sample concentration.
d	Sample thickness.
f	Count distribution (without instrumental bias).
k	Wave vector.
k_0	Light wave-vector.
m	Principal quantum number.
m_{e}	Effective electron mass.
n	Refractive index.
p	Pixels of the CCD camera.
r_{exc}	Exciton (electron-hole) radius.
s	Count distribution with instrumental bias.
t_0	Time zero.
t_∞	Time after excitation at which the samples raches a steady-state.
v	Vibrational quantum number.
v_{g}	Group velocity.
v_{k}	Kane velocity.
w_0	Distance between the two boundary rays of the gate.
e	Elementary positive charge.

Acknowledgments

At this point, I would like to thank all those who supported and motivated me during the preparation of this master thesis. I have learned an incredible amount and enjoyed this experience very much.

First of all, I would like to thank Prof. Julia Stähler and Prof. Beate Paulus, who supervised and reviewed my master thesis. I would like to thank both of them for their helpful suggestions, mentorship, and constructive criticism during the development of this thesis. I would also like to thank Prof. Julia Stähler for feedback on my writing and am grateful that her office door was always open whenever I ran into trouble.

Special thanks belong to Dr. Samuel Palato, without whom this work would not have been done. He not only introduced me to the FLUPS and supported me during the experiments but also assisted me with a lot of patience, interest, and willingness to help. Therefore, he contributed significantly that this thesis is available in this form.

Moreover, I would like to express my gratitude and appreciation for Prof. Niko Ernsting, whose guidance, encouragement, and expertise have been invaluable throughout this study.

In addition, the assistance and experience in ultrafast optics provided by Dr. Sergey Kovalenko were greatly appreciated.

I would like to thank all the electron dynamiX members, for the time spent together in the lab, in social settings, and online. I highly appreciate everyone in this group for so many things. Especially, I would like to thank Stefano Calati for the interesting debates and his ideas.

Finally, I would like to thank my close ones for their amity and support during my studies.

Statutory declaration

I hereby declare that I have written the present report independently. I have not used other than the declared sources. It has not been submitted to any examination body.

04.02.2022, signature